Sum-Of-Delay Models for Pressure Control in Water Distribution Networks

Giacomo Galuppini [a,*], Enrico Creaco[a], Lalo Magni[a]

[a]*Dipartimento di Ingegneria Civile e Architettura, University of Pavia, Pavia 27100, Italy*

Abstract

Service pressure control is a powerful tool to reduce leakage and risk of pipe bursts in Water Distribution Networks (WDNs). However, to obtain good control performances, it is essential to rely on a good model of the plant. A typical approach consists of the identification of a linear, local model of the system around the desired working point. Previous works relied on black-box, high order models to demonstrate that WDNs are characterised by a very complex dynamic behaviour, which should be properly modelled to avoid stability issues resulting from poor regulator design. This work aims at providing a physical justification for such complex dynamic behaviour, by means of a particular grey-box model structure, with pure delays as its fundamental blocks. Moreover, this works demonstrates that the new model structure can be very effective and efficient in modelling the WDN dynamics. Finally, to proper exploit the new model, this work proposes a bi-objective optimisation based procedure for the regulator design. The potentialities of both model identification and regulator design phases are assessed by means of simulated experiments performed on a detailed unsteady flow model of three different WDNs.

Keywords: WDN, RTC, PI, Time Delay, Smith Predictor

1. Introduction

In the recent years, the rise of the *Water 4.0* approach for the management of Water Distribution Networks (WDNs) has attracted the interests of both hydraulic and automatic scholar communities, with the final aim of developing and implementing new techniques to save water and energy [1]. New management techniques should exploit at best the new possibilities offered by the *Water 4.0* approach, such as the spread of smart sensors and actuators, connected to control units by means of high speed communication networks. New techniques include measuring and predicting users' water consumption [2, 3, 4], evaluating and improving WDN reliability [5, 6], monitoring and controlling water quality [7, 8].

Among new techniques, Real Time Control (RTC) of service pressure [9, 10, 11] plays a fundamental role, since it has been demonstrated to reduce water leakage [12, 13], risk of pipe burst [14, 15] and to extend the overall WDN infrastructure lifetime. Moreover, pressure RTC can be combined with higher level, optimal or predictive controllers designed for an optimised control of the whole WDN structure [16, 17, 18, 19, 20, 21, 22, 23], to further improve its management. Novel RTC techniques also allow to recover part of the energy by coupling standard Pressure Control Valves (PCVs) or Pressure Reducing Valves (PRVs) with Pump as Turbine (PAT) devices [24, 25, 26, 27], thus making RTC an even more interesting and profitable option for WDN managers. The problem of pressure RTC is typically faced with frequency domain control techniques [28, 29, 30], based on local, linear approximations of the WDN dynamics around the desired working point [28, 29]. However, the process typically moves away from its working point during operation, as a consequence of the time-varying nature of users' water demand. Due to the combined action of a strong process static gain nonlineairity, and a complex high frequency behaviour, this may result in instability of the closed-loop system [31]. As a crucial example, [32] describes an instability event occurred in a real WDN, due to the lack of understanding of the process dynamics, and a consequent poor control design. Such instability event had serious physical and financial consequences in terms of number of reported bursts at that time. A reliable process model is therefore essential for a proper tuning the regulator. The purpose of this work is then twofold: first, provide a physical-based justification for the complex high frequency dynamic of the plant, which was previously analysed by means of black-box models only [31, 33]. This result can be achieved by means of a particular grey-box model structure, based on the sum of pure delay contributions. Second, propose an optimisation-based procedure for the design of a regulator, built on top of the new model structure.

In particular, this work proposes a methodology for the computation of admissible delay values, based on the knowledge of structural WDN data only, and adopts a LASSO [34] approach for the selection of the most significant contributions and, at the same time, for the identification of free model parameters. This allows keeping the complexity of the model at a reasonable level, while retaining a sufficient amount of information about process dynamics. This paper also demonstrates that the new model structure can be effective and more efficient than stan-

*Corresponding author.
E-mail address: giacomo.galuppini01@ateneopv.it

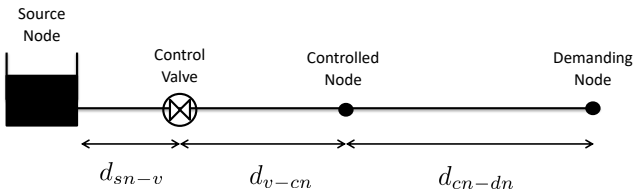

Figure 1: Case Studies A1 and A2. Topology of the water distribution systems.

dard, rational transfer functions, when the system step response shows a stair-shaped behaviour. As far as regulator tuning is concerned, this work follows the same rationale proposed in [35]: a bi-objective problem is setup, to express the trade-off between regulation performances and cost of control, while robustness of the design is taken into consideration by means of constraints on minimum robustness margins. The overall control scheme is implemented including a gain scheduling approach to further mitigate the effect of process gain non-lineariy on the closed-loop performance and robustness [36]. Simulations performed over a detailed numerical model of three different WDNs allows investigating the effectiveness and reliability of both model identification and regulator design.

This paper is organised as follows: § 2 describes the three WDNs adopted as Case Studies and the numerical modelling approach for the nonlinear WDN simulator; § 3 discusses in details the methodology for model identification through the computation of admissible delay values, and the use of LASSO for the identification of the free model parameters; § 3 also discusses the regulator design based on the solution of a bi-objective optimisation problem. Then, § 4 describes the application of the model identification procedure to the three Case Studies, and analyses the regulator design and test for the three Case Studies. Finally, § 5 discusses the overall results obtained with the proposed methodology, while § 6 formulates some concluding remarks.

2. Case studies and WDN unsteady flow model

In this work, three different Case Studies are adopted to demonstrate and discuss the identification of linear local models for the purpose of service pressure control, and their application in the design of linear regulators. This Section is therefore devoted to the description of the topology of the three WDNs adopted for simulations and of the specific control goals, as well as to a brief summary of the unsteady flow modelling methodology adopted to develop the simulation environment, which should describe the dynamics of the three systems in a highly accurate way and work as replacement of the real system to test the pressure control algorithms proposed in this work.

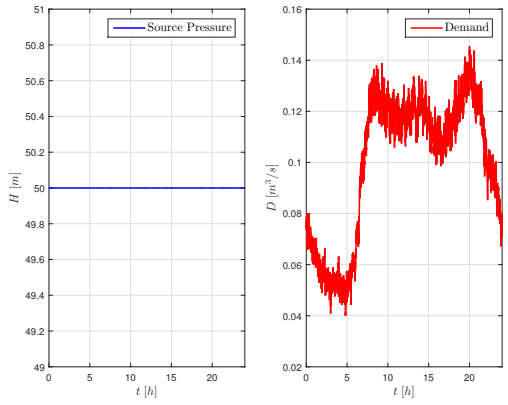

Figure 2: Case Studies A1 and A2. Source pressure and demand profile.

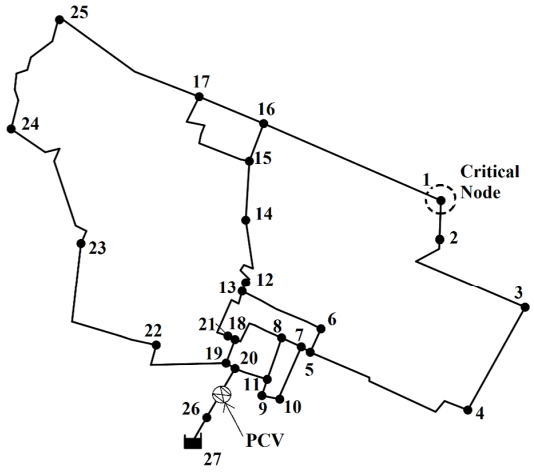

Figure 3: Case Study B. Topology of the WDN [3].

Case Studies A1 and A2, depicted in Figure 1, consists of WDNs with a simple topology, characterised by a single source node, connected to a single demanding node by means of a pipe. Actuation is obtained by means of a pressure control valve (PCV), whose closure speed is saturated for safety reasons. In particular, a full valve closure from the completely open position can be obtained in 100 s for this case study. The two topologies are characterised by the following distances:

- *Source node - Valve distance* d_{sn-v}, set to 250 m for Case Study A1, and 3000 m for Case Study A2, respectively.
- *Valve - Controlled node distance* d_{v-cn}, set to 4750 m for Case Study A1, and 1000 m for Case Study A2, respectively.
- *Controlled node - Demanding node distance* d_{cn-dn}, set to 5000 m for Case Study A1, and 6000 m for Case Study A2, respectively.

The temporal patterns of source pressure head and demand are depicted in Figure 2. No leakage is considered in this system.

Note that Case Studies A1 ad A2 are also exploited to test the design of pressure control algorithms based on the proposed

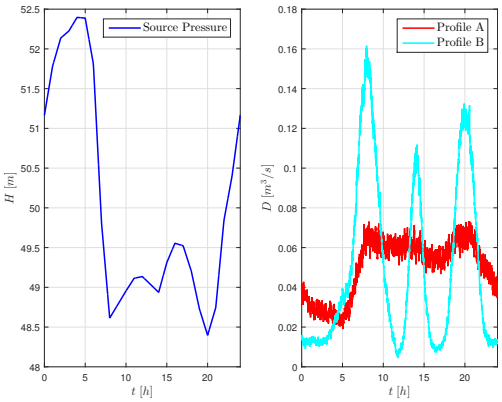

Figure 4: Case Study B. Source pressure and total demand profiles (sum of nodal demands across the WDN).

models. To this end, the range of available scenarios is extended by introducing two different offsets ($\{-0.03; 0.05\}$ $[m^3/s]$) in the demand profile, to cover a wider range of operating conditions and account for possible seasonal variation of the demand.

Case Study B is represented by the skeletonized WDN of the Italian town of Castelfranco Emilia (about 30,000 inhabitants). Actuation is obtained by means of a PCV installed in pipe 26-20 linking the source to the rest of the network, while pressure is measured at node 1, as depicted in Figure 3. The network consists of 26 demanding nodes with ground elevation of 0 m a.s.l. and 1 source node with ground level of 35 m a.s.l., and 32 pipes. For closed-loop simulations, two different demand patterns are considered for this case study, leading to two different trends of the total WDN demand (see Figure 4): a flatter trend (profile A) and a more peaked trend (profile B), sharing the same average values for each single demand profile. The source pressure head profile is reported in Figure 4 as well. A leakage percentage of 20% is also considered in this system. Note that PCV moves from a completely open to a completely closed position in 300 s.

Further details about the Case Studies can be found in [28, 36].

Remark: The choice of the three WDNs topologies is motivated by their different dynamic behaviours, as underlined by preliminary step responses experiment, depicted in Figures 5a, 5b, 5c. Note that step responses range from a clear stair shaped behaviour (Case Study A1) to a much smoother one, mainly exhibiting damped oscillations (Case Study B). This can be imputed to the three different network layouts, which result in different dominant physical phenomena. In particular, Case Studies A1 and A2 are characterised by a simple topology, and their dynamic behaviour is mainly determined by to wave reflection phenomena. In a real world scenario, these Case Studies approximate WDNs whose dynamics is strongly affected by that of its main water supply pipe. A stair-like behaviour is reported in different works in the pressure control literature [32, 37, 29, 31]. Notably, [32] reports an instability event recorded in a real plant due to a control design that was not properly handling such stair shaped dynamic behaviour, as discussed more in detail in [31, 33]. On the other hand, Case Study B is characterised by a complex topology and a very complex dynamic response, which is in this case caused by waves following different paths simultaneously and reaching the sensor at different time instants. As a result, this choice of the Case Studies allows investigating the proposed modelling and control methodologies in a wide range of realistic situations.

2.1. Numerical model

To carefully simulate dynamics of the Case Studies described earlier in this Section, a pressure-driven, nonlinear, unsteady flow modelling approach [38, 39, 40] is adopted, in order to allow a proper analysis of the hydraulic transients resulting from rapid nodal demand and/or valve setting variations. Moreover, to improve the accuracy of the model, pipe friction slopes are first computed according to the Darcy-Weisback formula, and then increased using the correction proposed by Pezzinga in [41], to account for the unsteady flow effects. In addition, for Case Study B, the presence of leakage from WDN pipes is considered by means of a pressure-dependent outflow. The effect of the control valve is modelled by considering no link at the valve site and setting nodal inflow at the upstream end Q_{up} and downstream end Q_{down} at:

$$Q_{up} = Q_{down} = \sqrt{\frac{2g}{\xi(\alpha)}} A \sqrt{\Delta H_{valve}} \tag{1}$$

where A $[m^2]$ is the valve cross-section area, g $[m/s^2]$ is the gravity acceleration constant, ξ is the valve head loss coefficient, ΔH_{valve} is the head drop in the valve and α is the valve closure setting, ranging from 0 (fully open) to 1 (fully closed). The valve head loss coefficient is a growing function of α. This function is typically made available by the valve manufacturer. Users'demand and tank pressure profiles are generated according to the bottom-up procedure, as described in [42, 43]. Finally, in order to obtain a more realistic framework, measurement noises $n_h(t)$ and $n_q(t)$ are introduced in the WDN model, acting respectively on the measured pressure $h(t)$, and on the flow at the valve site $Q(t)$.

3. Methodology

This Section focuses on a detailed description of the methodology, and is organised in three subsections, each one focusing on a different phase of the methodology. The first Subsection summarises the overall control design framework; the second Subsection introduces the main novelty of this work, i.e. the identification of a special class of linear models, composed of pure delays only, to describe the local dynamics of the system around the desired working point. Finally, the third subsection includes the new model structure in a bi-objective optimisation based approach for the design of a linear regulator.

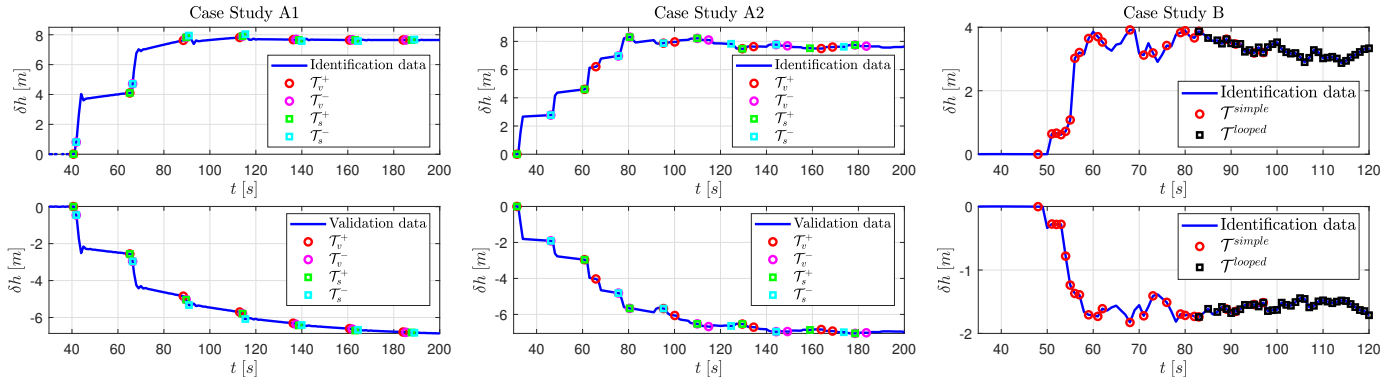

Figure 5: Step response output data $\delta h(t)$ (Top: identification data, Bottom: validation data) and admissible delays based on structural WDN information for Case Study A1 (a), Case Study A2 (b) and Case Study B (c).

3.1. Control framework

This Subsection summarises the key points of the $F^nPI - SP - gs$ control algorithm originally discussed in [36], which can be consulted for further details. The overall control scheme is depicted in Figure 6. For sake of compactness, in this work, the control algorithm will be referred to simply as F^nPI.

- *Definition of the nominal working point (WP) of the system.*
  Consider the overall Multi-Input Multi-Output (MIMO) system characterised by input signals $\xi(t)$, $H(t)$ and $D_i(t)$ (i.e. the local head loss coefficient ($[-]$), the source pressure head ($[m]$) and the water demand ($[m^3/s]$) at node i, respectively), and output signals $h(t)$ and $Q(t)$ (i.e. the pressure at the critical node of the WDN ($[m]$) and the flow at the valve site ($[m^3/s]$), respectively). In this scenario, the tuple $WP = (\overline{\xi}, \overline{H}, \overline{D}_1, ..., \overline{D}_{N_{nodes}}, \overline{h}, \overline{Q})$ describes the working point of the system.
  Note that average values of typical $H(t)$ and $D_i(t)$ profiles are usually available to the WDN manager, thus it is possible to consider such value as inputs to the system for the definition of the WP. Under this assumption, the value of ξ can be computed to obtain the desired pressure $h = h_{sp}$ at the controlled node. The values of the flow at the valve site Q is defined accordingly.

- *Identification of a linear, Single-Input Single-Output (SISO) model describing the system dynamics around WP.*
  Once the curve $\xi(\alpha)$ has been characterised, a transfer function $G(s)$, describing a SISO system with input signal $\delta\xi(t) = \xi(t) - \overline{\xi}$ and output signal $\delta h(t) = h(t) - \overline{h}$, can be identified from simulated step response experiments performed around WP. Note that the choice of ξ as the control variable is useful to compensate for a strong nonlinearity affecting the static gain of the process [36], which may endanger the stability of the closed-loop system when opearting far from WP, due to the presence of high frequency resonance peaks in $G(s)$ [31]. As stressed in [31], the knowledge of both frequency and height of such peaks is important to properly guide the phase of regulator tuning, which may otherwise rely on poor evaluations of robustness margins. The presence of resonance peaks was taken into account in [31, 36] with the identification of a black-box, high order transfer function with delay $G(s)$. This work proposes instead a class of gray-box linear models, whose structure is based the physics of the process under control. The values of the free parameters of the model can then be identified exploiting input-output data.

- *Nominal control design.*
  The nominal control design is based on the transfer function $G(s)$, and aims at regulating the pressure $h(t)$ to the setpoint h_{sp}, in presence of process disturbances generated by the effect of exogenous inputs $H(t)$ and $D_i(t)$. A Smith predictor is introduced to compensate for the effect of the main delay present in $G(s)$. As suggested in [35], the design phase can be carried out by solving a bi-objective optimisation problem, with objective functions considering the product of static gain and critical frequency of the loop function $L(s)$ on one hand, and the attenuation of resonance peaks on the other hand. The tuning procedure, which was originally developed for standard transfer function models, is extended to allow for the use of the novel model structure proposed in this work.

- *Discretisation.* All transfer functions involved in the control scheme are discretised by means of *Tustin* method, to preserve their stability properties, with a proper sampling time according to Nyquist sampling theorem [44].

- *Definition of a nonlinearity inversion block and a gain scheduling policy for the regulator static gain.*
  A nonlinearity inversion block is introduced in the control loop to compute, at each time instant, the value of α that corresponds to the valve head loss coefficient ξ required by

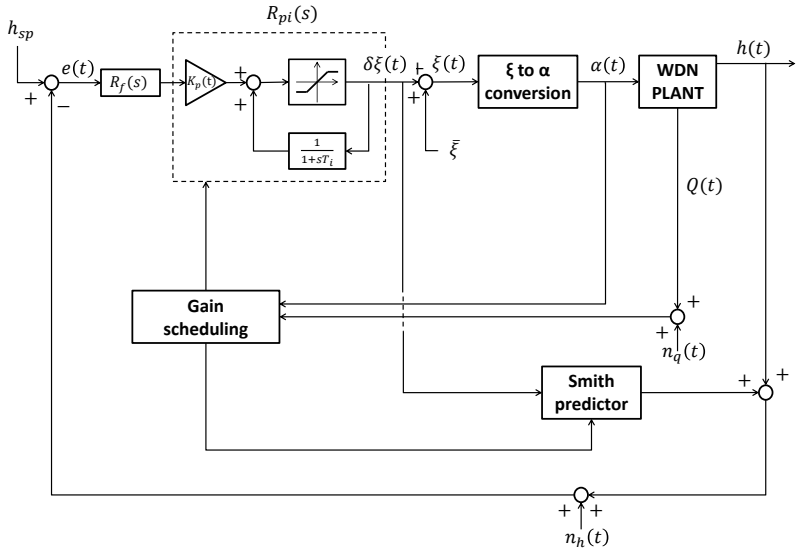

Figure 6: Complete block scheme for the $F^nPI-SP-gs$ control algorithm including: the unitary gain filter $R_f(s)$, a Proportional-Integral regulator with antiwindup implementation $R_{pi}(s)$, the nonlinearity inversion block ξ *to* α *conversion* for the online computation of the valve closure α corresponding to the desired local head loss coefficient ξ, the WDN plant (simulated according to the unsteady flow modelling described in § 2.1), a Smith predictor for the compensation of the main process delay, and gain scheduling policies for the online gain adaptation of the Smith predictor and of the regulator, based on the valve closure α and on the measured values of flow at the valve site $Q + n_q$.
The main signals in the loop are: the pressure setpoint $h_{sp}(t)$, the error signal $e(t)$, the control action (local head loss coefficient variation) $\delta\xi(t)$, the equilibrium input (equilibrium local head loss coefficient) $\bar{\xi}$, the overall local head loss coefficient $\xi(t)$, the valve closure $\alpha(t)$, the pressure at the controlled node $h(t)$, the measurement noise acting on the pressure $n_h(t)$, the flow at the valve site $Q(t)$, the measurement noise acting on the pressure $n_q(t)$.

the regulator. Moreover, based on the availability of real time measurements of Q and α, a gain scheduling policy for $R(s)$ can be introduced to further improve the robustness of the control scheme, and balance between cost of control and regulation error. Further details can be found in [36].

3.2. Sum-of-Delays models identification

This Section introduces the class of Sum-of-Delays (SOD) models and discusses the identification of its free parameters from structural data of the WDN under consideration, and from input-output data obtained from simulated step response experiments.

Let s be the *Laplace* variable. In the *Laplace* domain, a SOD, SISO transfer function model is defined as follows:

$$G(s) = \frac{Y(s)}{U(s)} = \sum_{p=1}^{P} \mu_p e^{-s\tau_p} \tag{2}$$

$$\tau_1 < \tau_2 < ... < \tau_P \tag{3}$$

with $U(s)$ and $Y(s)$ the *Laplace* transforms of generic system input and output $u(t)$ and $y(t)$, respectively. The corresponding time domain impulse response results:

$$y(t) = \sum_{p=1}^{P} \mu_p u(t - \tau_p) \tag{4}$$

Note that the unitary step response of a SOD model results in a stair-shaped response, with the output $y(t) = 0$ for $t < \tau_1$, $y(t) = \mu_1$ for $\tau_1 \leq t < \tau_2$, $y(t) = \mu_1 + \mu_2$ for $\tau_2 \leq t < \tau_3$, and so on. A single step variation of the input signal results in multiple step variations, which only commute the output after determined time intervals. This reflects the dynamics of wave propagation through a WDN, where pressure perturbation waves travel through pipes at finite speed (celerity c) and can trigger a reflected wave when reaching WDN nodes. As the wave travels along the pipes, it looses energy due to friction. Once the topology of the WDN and the speed of pressure waves are known, it is then possible to directly compute a finite set of delay values $\{\tau_1, ..., \tau_P\}$ to be included in the model, with P sufficiently high to capture all the significant contributions. The physically-based computation of delays is now presented for the two different WDN topologies adopted as Case Studies.

3.2.1. Physically-based computation of delays, Case Study A1 and A2

Consider the simple topology of Case Studies A1 and A2, depicted in Figure 1, with the associated characteristic distances (d_{sn-v}, d_{v-cn} and d_{cn-dn}) as introduced in § 2. Let also assume the value of the celerity c to be known from Equation 52, reported in § A. A step pressure perturbation, generated by closure or opening valve manoeuvres at time $t = 0$, travels through the pipe at speeds $\pm c$. Let consider the wave travelling at positive speed first. Such wave affects the measured pressure after a time $t = \tau_1^+ = d_{v-cn}/c$. The wave then progresses to the demanding node, where a reflected wave is generated, whose am-

plitude is affected by the incident wave and the boundary condition. The reflected wave travels back and affects the measured pressure after a time $t = \tau_2^+ = \tau_1^+ + 2d_{cn-dn}/c$, and reaches back the valve, where part of the wave is reflected, and affects again the pressure measure at a time $t = \tau_{v3}^+ = \tau_2^+ + 2d_{v-cn}/c$, while part can keep on travelling towards the source node, where it is reflected. Such reflected wave is partially reflected back by the valve, and partially affect the measured pressure at a time $t = \tau_{s3}^+ = \tau_2^+ + 2(d_{v-cn} + d_{sn-v})/c$, and so on. A similar dynamics characterises the wave that originally started travelling at speed $-c$. Note that each time a pressure wave reaches the valve, it splits into two waves travelling at opposite speeds. From a practical viewpoint it is then convenient to consider a subset of all possible waves. In this work, the following waves are considered, along with the corresponding delays:

- $\mathcal{T}_v^+$, i.e. the set of delays associated with waves that start propagating with positive speed, and get reflected by the valve from the downstream end.
- $\mathcal{T}_s^+$, i.e. the set of delays associated with waves that start propagating with positive speed, cross the valve and get reflected by the source node.
- $\mathcal{T}_v^-$, i.e. the set of delays associated with waves that start propagating with negative speed, and get reflected by the valve from the downstream end.
- $\mathcal{T}_s^-$, i.e. the set of delays associated with waves that start propagating with negative speed, cross the valve and get reflected by the source node.

Moreover, due to friction, the number of waves travelling trough the pipe remains finite, the effect of waves on the measured pressure reduces with the travelled distance, and the step response eventually settles to a steady state value. The analysis of the system step response allows definition of a time limit t_{max}, after which the effect of pressure waves is negligible. Once t_{max} is defined, each delay set can be populated by iteratively adding delay contributions, until the computed delay value overcomes t_{max}. For example, the elements of $\mathcal{T}_v^+$ can be computed as:

$$\tau_{v1}^+ = d_{v-cn}/c \tag{5}$$
$$\tau_{v2}^+ = \tau_1^+ + 2d_{cn-dn}/c \tag{6}$$
$$\tau_{v3}^+ = \tau_2^+ + 2d_{v-cn}/c \tag{7}$$
$$... \tag{8}$$

while the elements of $\mathcal{T}_v^-$ can be computed as:

$$\tau_{v1}^- = (2d_{sn-v} + d_{v-cn})/c \tag{9}$$
$$\tau_{v2}^- = \tau_1^- + 2d_{cn-dn}/c \tag{10}$$
$$\tau_{v3}^- = \tau_2^- + 2d_{v-cn}/c \tag{11}$$
$$... \tag{12}$$

The overall set of admissible delay values is:

$$\mathcal{T}^a = \mathcal{T}_v^+ \bigcup \mathcal{T}_s^+ \bigcup \mathcal{T}_v^- \bigcup \mathcal{T}_s^- \tag{13}$$

Note that duplicate delay values may appear in different delay classes, and the cardinality of $\mathcal{T}^a$ is lower than the sum of the four cardinalities of delay classes.

3.2.2. Physically-based computation of delays, Case Study B

Consider the complex topology of Case Study B, depicted in Figure 3, and assume the value of the celerity c to be known from Equation 52, for each pipe of the WDN. A step pressure perturbation, generated by closure or opening valve manoeuvres at time $t = 0$, can split in multiple waves which travel through the WND pipes and reach the controlled node through multiple paths. Moreover, once each wave has reached the controlled node, it can keep travelling and reach again the controlled node through other different paths, until friction reduces the perturbation that propagates as wave to a negligible value. In this scenario, a weighted graph can be constructed, with graph nodes corresponding with WDN nodes, graph edges corresponding with WDN pipes and edge weights corresponding to pipe travel times, with the travel time of the $i-th$ pipe tt_i defined as:

$$tt_i = \frac{L_i}{c_i} \tag{14}$$

with L_i the length of the i-th pipe, and c_i the wave celerity through the i-th pipe. In this framework, the PCV is replaced by a dummy pipe connecting two dummy nodes, while the corresponding travel time is set at a negligible value. The graph representation allows exploiting path-search algorithms to compute set of admissible delay values (i.e. the overall travel time of each path). For instance, let define two delay sets as follows:

- $\mathcal{T}^{simple}$, i.e. the set of delays associated with waves that reach the controlled node through simple, loop-less paths.
- $\mathcal{T}^{looped}$, i.e. the set of delays associated with waves that reach the controlled node through looped paths.

Yen's k-shortest path algorithm [45] can be straightforwardly exploited to compute the elements of $\mathcal{T}^{simple}$. A possibility to compute the elements of $\mathcal{T}^{looped}$ is to modify the weighted graph by introducing a dummy controlled node and a dummy edge (of negligible travel time), between the controlled node and a neighbouring node. Then, a further delay set $\mathcal{T}^{cycles}$ can be defined as the set of delays associated with loop-less paths starting from the controlled node and reaching the dummy controlled node. Again, Yen's algorithm can be used to compute delays. Finally, the elements of $\mathcal{T}^{looped}$ can be computed starting from $\mathcal{T}^{simple}$ and $\mathcal{T}^{cycles}$, by combining (summing) each element of $\mathcal{T}^{simple}$ with all elements of $\mathcal{T}^{cycles}$. The procedure can be iterated to further extend the set of admissible delays.

The overall set of admissible delay values is:

$$\mathcal{T}^a = \mathcal{T}^{simple} \bigcup \mathcal{T}^{looped} \tag{15}$$

Note that duplicate delay values may appear in different delay classes. Moreover, a preliminary analysis of the system step response allows to define a time limit t_{max}, after which the effect of pressure waves is negligible, to reduce the cardinality of $\mathcal{T}^a$.

Remark: One of the goals of this work is providing a physical interpretation for the complex, high frequency process dynamics that may impact on closed-loop stability [31]: this motivates the choice of computing $\mathcal{T}^a$ from structural data of the WDN. However, in practice, when the step response of the WDN around WP shows a clear, stair-shaped behaviour, it may be possible to define $\mathcal{T}^a$ by direct inspection of step response data.

3.2.3. Identification of free model parameters

Once delay values τ_p are available, the only free parameters are the associated gains μ_p, whose values can be identified by means of input-output identification. As anticipated earlier in this work, step response experiments performed around the desired WP allow gathering input-output data for the purpose of model identification. In this case, the input signal to the SOD model is then $u(t) = \delta\xi(t) = \xi(t) - \overline{\xi}$, while its output is $y(t) = \delta h(t) = h(t) - \overline{h}$. Note that, assuming a sampling time T_s for experimental data, pressure commutations can only occur at time instants that are integer multiples of T_s. For this reason, it is convenient to round the delay values of $\mathcal{T}^a = \{\tau_1^a, \tau_2^a, ...\}$ to be multiples of T_s (thus further reducing the cardinality of the set), and move to a discrete-time notation. Let the corresponding discrete-time delay set be defined as $\mathcal{T}^d = \{\tau_1^d, \tau_2^d, ...\tau_P^d\}$, with:

$$\tau_p^d = round(\frac{\tau_p}{T_s}) \tag{16}$$

Remarkably, if the values of the delays are all known, the SOD model in its discrete-time domain formulation is linear with respect to parameters μ_p. It is in fact possible to assume that the input is applied at the discrete time instant $k = 0$, and write the problem in the form:

$$\mathbf{\Psi} = \mathbf{\Phi\Theta} \tag{17}$$

with $\mathbf{\Psi}$ a $N \times 1$ vector containing the output samples, $\mathbf{\Phi}$ a $N \times P$ matrix containing the delayed input samples, and $\mathbf{\Theta}$ a $P \times 1$ vector containing the gain associated to each delay. In this case, a simple Least Squares (LS) estimation [34] can be adopted to derive the optimizer $\mathbf{\Theta}^\star$. However, due to the high dimensionality of the parameter space (i.e. the number of possible delays), the straightforward use of this technique is likely to result in overfitting of identification data. To overcome the problem, a LASSO [34] approach is adopted in this work, i.e.:

$$\mathbf{\Theta}^\star = arg\min_{\mathbf{\Theta}} ||\mathbf{\Psi} - \mathbf{\Phi\Theta}||_2^2 + \lambda||\mathbf{\Theta}||_1 \tag{18}$$

with λ a tuning parameter. Note that the *norm-1* regularisation term $\lambda||\mathbf{\Theta}||_1$, added to the standard LS cost function, has the effect of forcing some of the coefficient estimates to be exactly equal to zero when the tuning parameter λ is sufficiently large (with other norm penalties, such as norm-2 in Ridge Regression, some coefficient estimates may approach zero but never reach it) [34]. Hence, the LASSO can be exploited to perform variable selection and reduce the complexity of the final model.

The choice of λ is typically based on a comparison of the model performances with both an identification and a validation dataset, according to proper *goodness of fit* metrics. In the context of this work, the choice is based on the Root Mean Squared Error (RMSE):

$$RMSE = \sqrt{\frac{||\mathbf{\Psi} - \mathbf{\Phi\Theta}||_2^2}{N}} \tag{19}$$

Other useful metrics are:

$$FIT = 1 - \frac{||\mathbf{\Psi} - \mathbf{\Phi\Theta}||_2}{||\mathbf{\Psi} - mean(\mathbf{\Psi})||_2} \tag{20}$$

$$COD = = 1 - \frac{||\mathbf{\Psi} - \mathbf{\Phi\Theta}||_2^2}{||\mathbf{\Psi} - mean(\mathbf{\Psi})||_2^2} \tag{21}$$

In particular, RMSE, COD and FIT metrics are adopted in this work for the evaluation of the model performances with a test dataset, obtained from simulations of realistic valve trajectories.

Finally, since regulator tuning is performed in the *Laplace* domain, it is possible to compute approximate continuous-time delay values as follows:

$$\tau_p = \tau_p^d T_s \tag{22}$$

$$\forall\ p = 1, 2, ..., P \tag{23}$$

and construct the corresponding SOD transfer function model as in Eq. (2).

As discussed more in details in the reminder of this work, the interaction of multiple pure delay contributions determines, in the Bode diagram of $G(s)$ magnitude, a number of resonance peaks, with peaks corresponding to in-phase interactions, and valleys to counter-phase interactions.

Remark: It is worth noting that the discrete time, sum-of-delay model:

$$y(k) = \sum_{p=1}^{P} \mu_p u(k - \tau_p^d) \tag{24}$$

can be interpreted as a *sparse* version of a general impulse response model:

$$y(k) = \sum_{i=0}^{I} g_i u(k - i) \tag{25}$$

with k the discrete time instant, $I = \tau_P^d$, and where the impulse response coefficients g_i that are related to physically inadmissible output commutations are constrained to zero. Since the relevant information regarding the local frequency response of the system is mainly encoded in the sharper jumps of the step response, the model can be sparsified without any significant loss of information. Note that the use of LASSO, opposed to the standard LS approach, further explores this direction. Finally, note that the maximum number of admissible delays can be made arbitrarily large, without any loss of generality.

3.3. Regulator design

This Section describes how to adapt the bi-objective tuning procedure originally developed in [35] to SOD, *Laplace* domain transfer functions. The proposed optimisation-based design of loop functions is particularly useful in case of SOD models, since it does not directly rely on the singularities of $G(s)$, but refers more in general to the shape of magnitude and phase Bode diagrams of the loop function.

3.3.1. Smith predictor

Previous works [28, 31] highlighted the benefits of the introduction of a Smith predictor in the control scheme, with the aim of reducing the effect of pure delay on the control loop. Let $H(s)$ be the product of a rational transfer function $H'(s)$ and a single pure delay, i.e. $H(s) = e^{-s\tau}H'(s)$. Under these assumptions, the Smith predictor transfer function $P(s) = (1 - e^{-s\tau})H'(s)$ can be derived by requiring $H(s) + P(s) = H'(s)$. This allows neglecting the presence of the delay in the regulator tuning.

With the proposed SOD transfer function models, a possibility is to design the Smith predictor on a simplified model $G_p(s)$, describing the low frequency behaviour of the plant around the working point. A possible choice, which does not require any additional model identification phase, is:

$$G_p(s) = e^{-s\tau_1}G(0) \tag{26}$$

Note that τ_1 is the shortest time delay of $G(s)$, while $G(0)$ corresponds to its static gain. Then one can derive the Smith predictor as follows:

$$P(s) = (1 - e^{-s\tau_1})G(0) \tag{27}$$

The regulator tuning can then be performed with reference to the new process transfer function $G'(s) = G(s) + P(s)$.

Remark: While the above procedure does not allow fully neglecting the presence of the first delay of $G(s)$, it allows compensating its effect in a sufficient frequency range. This can be reasonable since, to obtain resonance peak deamplification, the closed-loop bandwidth must always be placed at lower frequency than those of the resonance peaks. Moreover, the proposed approach explicitly accounts for the residual phase margin reduction due to the model mismatch at higher frequencies in the design phase of the regulator.

3.3.2. Bi-objective optimisation based regulator design

Let $G'(s)$ be a general, asymptotically stable process transfer function. Let μ_g be its static gain, and let $\mathcal{W}_{rp} = \{\omega_{rp_1}, \omega_{rp_2}, ...\}$ be the set of frequencies associated with $G'(s)$ resonance peaks.

A F^nPI regulator transfer function is given by:

$$R(s) = R_{pi}(s)R_f(s) \tag{28}$$

with:

$$R_{pi}(s) = \mu_r \frac{1 + sT_i}{s} \tag{29}$$

$$R_f(s) = \frac{\prod_{i=1}^{n}(1 + sT_{d_i})}{\prod_{i=1}^{n}(1 + sT_{f_i})} \tag{30}$$

Note that $R(s)$ represents the cascade of a Proportional-Integral regulator $R_{pi}(s)$ and a unitary gain filer $R_f(s)$, with order n and zero relative degree.

Let $\boldsymbol{X}$ be the vector of optimisation variables:

$$\boldsymbol{X} = [\mu_r \;\; T_i \;\; T_{f_1} \;\; ... \;\; T_{f_n} \;\; T_{d_1} \;\; ... \;\; T_{d_n}]' \tag{31}$$

It holds then:

$$L(s, \boldsymbol{X}) = R(s, X)G'(s) \tag{32}$$

In particular, let $\mu_L(\boldsymbol{X}) = \mu_r\mu_g$ be the static gain of $L(s, \boldsymbol{X})$, and $\mathcal{W}_c = \{\omega_{c_1}, \omega_{c_2}, ...\}$ be the set of crossover frequencies, i.e. $\omega_c \in \mathcal{W}_c \; if \; |L(j\omega_c, \boldsymbol{X})| = 1$. Finally, let $\mathcal{W}_\pi = \{\omega_{\pi_1}, \omega_{\pi_2}, ...\}$, with $\omega_\pi \in \mathcal{W}_\pi \; if \; arg(L(j\omega_\pi, \boldsymbol{X})) = -180°$.

The following robustness indicators [46] can be introduced:

- *Phase margin*: $\phi_m = 180° - |argL(j\omega_c^\star, \boldsymbol{X})|$, with $\omega_c^\star = arg\min_{\omega_c \in \mathcal{W}_c} |L(j\omega_c, \boldsymbol{X}) + 1|$.
- *Gain margin*: $K_m = 1/|L(j\omega_\pi^\star, \boldsymbol{X})|$, with $\omega_\pi^\star = arg\min_{\omega_\pi \in \mathcal{W}_\pi} |L(j\omega_\pi, \boldsymbol{X}) + 1|$.
- *Vector margin*: $\Delta_m = \min_\omega |1 + L(j\omega, \boldsymbol{X})|$,

Assume a single crossover frequency $\omega_c^\star$ exists for $L(s, \boldsymbol{X})$. Then two objective functions can be defined as follows:

$$J_1(\boldsymbol{X}) = -|\mu_L(\boldsymbol{X})\omega_c^\star(\boldsymbol{X})| \tag{33}$$

$$J_2(\boldsymbol{X}) = \max_{\omega_{rp} \in \mathcal{W}_{rp}} (|L(j\omega_{rp}, \boldsymbol{X})|) \tag{34}$$

with $-J_1$ the *Gain-Bandwidth Product* (GBP) and J_2 the *Maximum Peak Height* (MPH).

The *Regulator Tuning Bi-Objective Optimisation Problem* (RT-BOOP) is then given by:

$$\min_{\boldsymbol{X}}(J_1(\boldsymbol{X}), J_2(\boldsymbol{X})) \tag{35}$$

subject to:

$$\mu_L(\boldsymbol{X}) > 0 \tag{36}$$

$$\mathbf{card}(\mathcal{W}_c) = 1 \tag{37}$$

$$\phi_m(\boldsymbol{X}) > 0 \tag{38}$$

$$\phi_m(\boldsymbol{X}) \geq \underline{\phi_m} \tag{39}$$

$$k_m(\boldsymbol{X}) \geq \underline{k_m} \tag{40}$$

$$\Delta_m(\boldsymbol{X}) \geq \underline{\Delta_m} \tag{41}$$

$$\max_{\omega_{rp} \in \mathcal{W}_{rp}} (|L(j\omega_{rp}, \boldsymbol{X})|) \leq \overline{L}_{rp} \tag{42}$$

$$T_i, T_{f_1}, ..., T_{f_n}, T_{d_1}, ..., T_{d_n} > 0 \tag{43}$$

with $\underline{\phi_m} > 0$, $\underline{k_m} > 1$, $\underline{\Delta_m} > 0$, $\overline{L}_{rp} < 1$, and **card**$(\cdot)$ denoting the set cardinality operator.

Remark: Note that the RT-BOOP formulation proposed in this work differs from the original one for constraints (37-38). In fact, while the original formulation relies on a direct computation of closed-loop poles to force closed-loop stability, the new formulation enforces it by means of *Bode criterion* (reported in § C) [44], the hypotheses of which are guaranteed by constraints (36-38). This avoids any use of transfer function singularities and allows relying on the shape of Bode diagrams only, thus making RT-BOOP suitable to deal with SOD models.

RT-BOOP can be solved by means of a Multi-Objective Genetic Algorithm, such as NSGA-II Genetic Algorithm [47]. Constraints are implemented as *soft constraints*, with a static penality function, as suggested in [48]. Higher penalties are introduced for stability constraints (36-38), with respect to robustness and performance ones. This also motivates the presence of constraint (38), which otherwise appears to be redundant due to constraint (39). The solution of RT-BOOP via NSGA-II Genetic Algorithm is a finite dimension set of feasible solutions, approximating the Pareto optimal front. The designer can then select the desired tuning among the possible solutions, according to both expected performances and, possibly, further considerations regarding the process under control. For further details, refer to [35].

3.3.3. LP-filtered Sum-of-Delay models

It must be remarked that the introduction of a simple first order, unit gain, low-pass action $G_2(s) = 1/(1 + sT_g)$ in the process model may help improving the regulator tuning process via RT-BOOP, which can be performed based on $G'(s) = G(s)G_2(s)$.

In case of Smith predictor, one can set:

$$P(s) = (1 - e^{-s\tau_1})\frac{G(0)}{(1 + sT_g)} \tag{44}$$

and tune the regulator based on $G'(s) = G(s)G_2(s) + P(s)$. The filtering pole can be placed at the Nyquist frequency $\omega_N = \pi/T_s$, to account for the high-frequency cutoff effect of the sample and hold procedure. Note that, in case ω_N is too low in frequency, this may introduce some phase margin reduction which may not necessarily coincide with that of a sample and hold. Another possibility is to exploit experimental data and identify T_g by means of input-output identification techniques.

4. Application

This Section describes the identification of SOD models for Case Studies A1, A2 and B. For sake of comparison, high order rational transfer function models are also identified. Moreover, *PI* and F^1PI regulators are tuned by means of RT-BOOP, based on the SOD transfer function models. Identification data are obtained from simulations of the open-loop response three Case Studies, according to the nonlinear, unsteady flow model described in § 2.1. The same simulation environment is then used as replacement for the real WDN for the evaluation of regulator performances.

p	τ_p	μ_p
1	12	-0.01
2	36	-0.008
3	37	-0.0013
4	59	-0.0007

Table 1: Case Study A1. Delays and coefficients of SOD model obtained via LASSO.

Model	*RMSE*	*FIT*	*COD*
SOD via LS	1.202	0.819	0.962
SOD via LASSO	1.187	0.82	0.963
Rat. TF with Delay	1.818	0.822	0.963

Table 2: Case Study A1. Goodness of fit metrics for the Test dataset.

4.1. Model identification

4.1.1. Case Study A1

The control goal for Case Study A1 is regulation of the measured pressure to a setpoint $h_{sp} = 29\ m$. The corresponding WP results:

$$WP_{A1} = \begin{cases} \overline{\xi} = 871\ (i.e.\ \overline{\alpha} = 0.694) \\ \overline{H} = 50\ m \\ \overline{D}_1 = 0.1\ m^3/s \\ \overline{h} = 29\ m \\ \overline{Q} = 0.1\ m^3/s \end{cases} \tag{45}$$

Step response experiments are performed around WP_{A1} to collect data and construct an identification and a validation dataset. Moreover, test data are collected by simulating a realistic valve trajectory around the working point. The three datasets are depicted in Figures 7a, 7b, 7c.

The first step of the identification procedure for SOD models is the definition of admissible delay values, based on structural information regarding the WDN under consideration. For Case Study A1, the topology is described in § 2 and depicted in Figure 1. Pressure wave celerity can be computed by means of Eq. (52), and results $c = 407.9\ m/s$. The application of the methodology proposed in § 3.2.1 allows to compute the sets $\mathcal{T}_v^+$,$\mathcal{T}_v^-$,$\mathcal{T}_s^+$,$\mathcal{T}_s^-$. Figure 5a highlights the computed delay values over the step responses output data. Note that all the major pressure commutations occur very close to the expected commutation times computed from the WDN topology. As expected, τ_v^+ and τ_s^+ values coincide for the first two values, and then slowly start dephasing due to the further distance d_{sn-v} the wave associated with τ_s^+ has to travel. The same holds for τ_v^- and τ_s^- values.

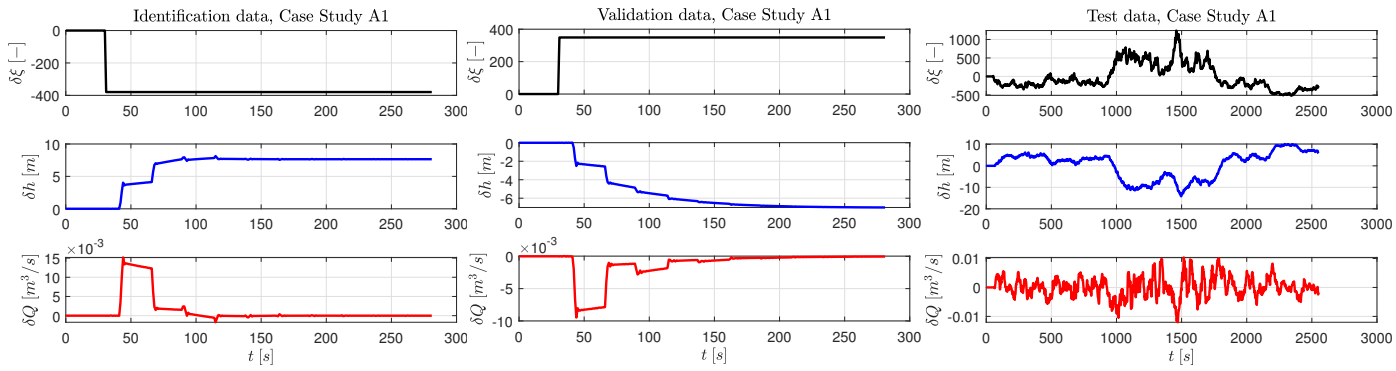

Figure 7: Case Study A1. Model identification (a), validation (b) and test (c) data from step response experiments. Top, black line: valve head loss coefficient deviation from equilibrium value $\delta\xi(t)$; middle, blue line, measured pressure variation from equilibrium value $\delta h(t)$; bottom, red line: flow at the valve site variation from equilibrium value $\delta Q(t)$.

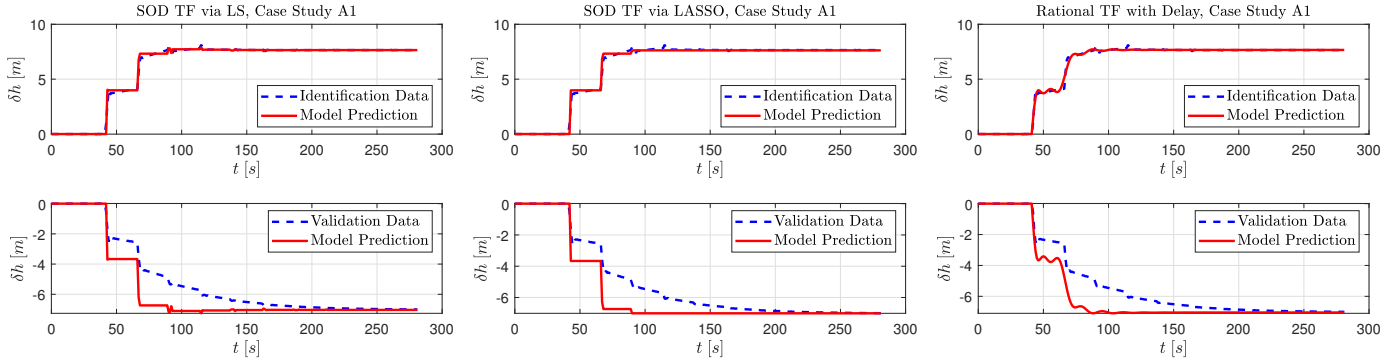

Figure 8: Case Study A1. Comparison of pressure data and model predicted pressure (Top: identification, Bottom: validation), for SOD model obtained via LS (a), SOD model obtained via LASSO (b), rational transfer function with delay (c).

Note that many contributions affect the measured pressure almost simultaneously, and the overall step response is composed of few, step-shaped contributions, despite the high number of effective contributions. With a black-box approach, a small set of admissible delay values could be defined by inspection of the step response pressure signal. Once admissible values $\mathcal{T}^a$ are available, the set of discrete-time admissible delay values $\mathcal{T}^d$ can be constructed, and the associated gains identified via LS. To reduce the complexity of the model, a LASSO approach can be adopted, as described in the previous Section. Different models are identified, with different values of the shrinkage parameter λ. The final one is then chosen by inspecting the RMSE trend for both identification and validation, as function of λ. As shown by Figure 9a, both identification and validation RMSE share a similar trend, and settle to steady values for $\lambda \leq 10$. The choice of $\lambda = 10$ results in the model parameters reported in Table 1. For sake of comparison, a standard rational transfer function with a single delay value is also identified, relying on Matlab System Identification Toolbox [49]. The choice of the system order follows the same rationale adopted for the choice of λ: Figure 9b depicts the trend of identification and validation RMSE for different system orders. Note that, while the validation RMSE trend is almost flat regardless of the system order, the identification one almost settles from order 7, which is chosen as final system order.

Figures 8a, 8b and 8c show a comparison of pressure data and model predicted pressure for both identification and validation datasets, for the three different models. Note that LS model prediction closely follows the identification data, even in its minor commutations (see for example at time $t \approx 85$ s), while LASSO model prediction only follows its main commutations. The same holds for the rational transfer function with delay, which tries to reproduce the stair shaped signal by introducing small oscillations. In all cases, the mismatch between data and model predictions for the validation case can be imputed to a different system dynamics between valve opening and closing, which results in a smoother step response. The static gain is correctly estimated by all the three models, for both identification and validation data. Figure 10a shows a comparison of test data and model predictions. All three models well reproduce most of the test data, while overestimating the response around $t = 1500$ s. This is mainly due to a variation in the flow Q, which affects the process static gain and, partially, process dynamics. However, recall that this effect is taken into account in the overall control scheme with an appropriate gain scheduling policy [36]. FIT and COD values for test data are reported in

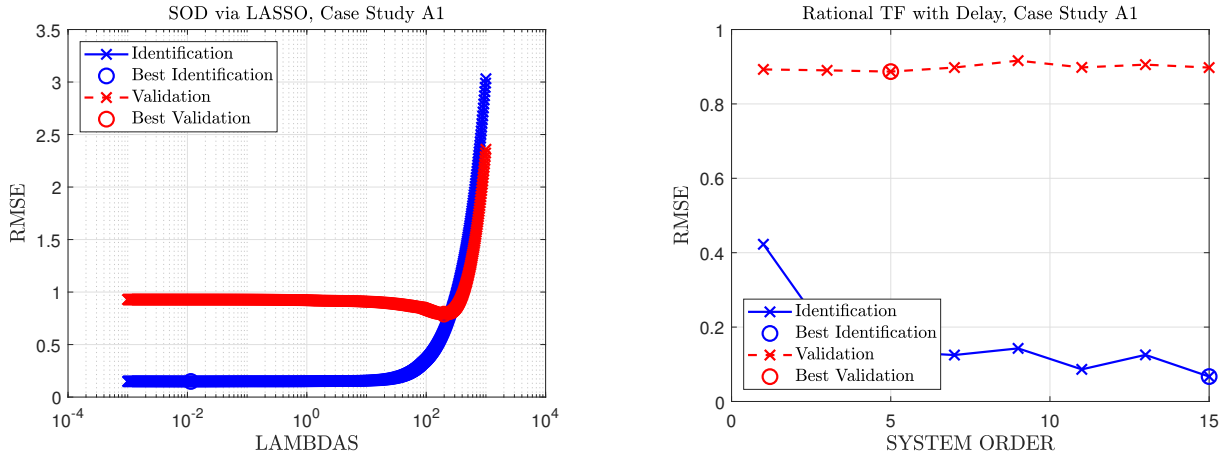

(a) (b)

Figure 9: Case Study A1. Comparison of identification (blue, solid line) and validation (red, dashed line) RMSE, for SOD models obtained via LASSO (a), and comparison of identification (blue, solid line) and validation (red, dashed line) RMSE for rational transfer functions with delay (b).

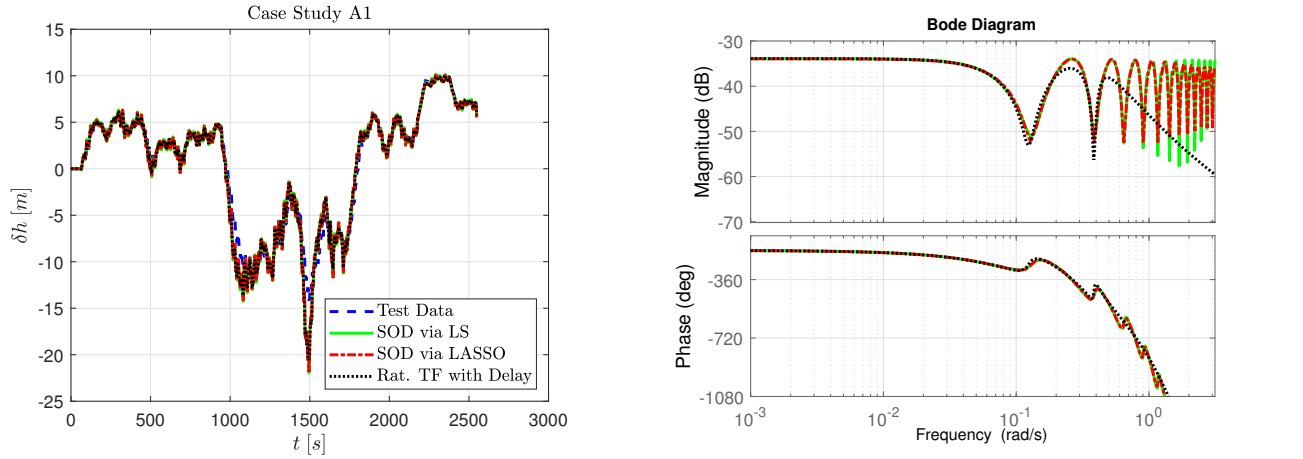

(a) (b)

Figure 10: Case Study A1. Comparison of test data (blue, dashed line), predictions for SOD model obtained via LS (green, solid line), SOD model obtained via LASSO (red, dotted-dashed line), rational transfer function model with delay (black, dotted line) (a). Comparison of Bode diagrams, depicted up to the Nyquist frequency (b).

Table 2. Figure 10b shows instead a comparison of the Bode diagrams of the three models, depicted up to the Nyquist frequency. Note that both SOD models share a very similar diagram for both magnitude and phase, with a number of resonance peaks appearing at high frequency, due to the interaction of delayed contributions. The rational transfer function with delay tries to approximate this shape, starting from peaks located at lower frequencies. It would be possible to show that, as the system order increases, peaks located at higher frequencies are included in the dynamic description of the process. Remarkably, the SOD model obtained via LASSO provides very similar information about the process dynamics with few free parameters, while the other models require a higher complexity to properly describe the high frequency dynamic behaviour of th WDN around WP.

p	τ_p	μ_p
1	2	-0.00750
2	17	-0.00440
3	31	-0.00440
4	36	-0.00210
5	46	-0.00150

Table 3: Case Study A2. Delays and coefficients of SOD model obtained via LASSO.

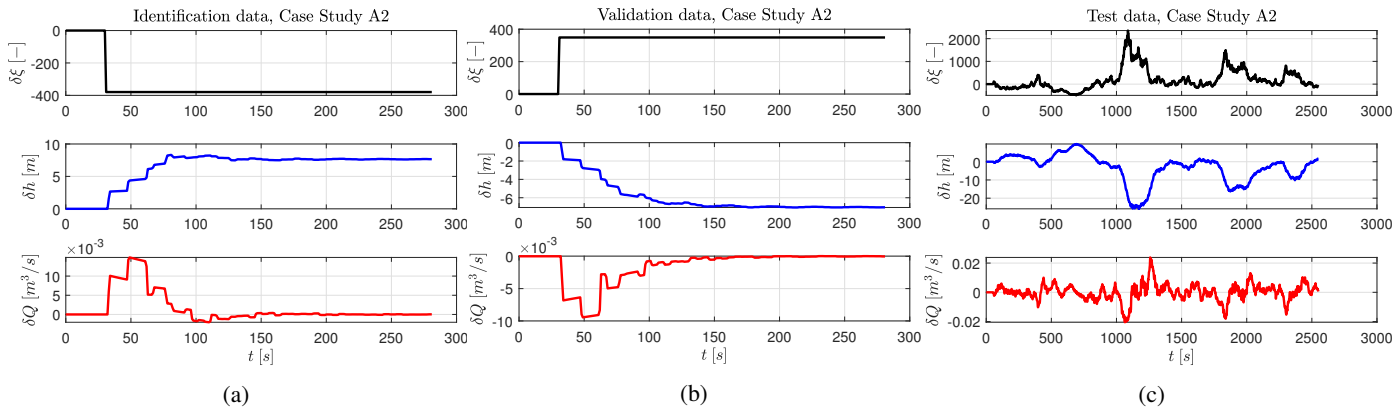

Figure 11: Case Study A2. Model identification (a), validation (b) and test (c) data from step response experiments. Top, black line: valve head loss coefficient deviation from equilibrium value $\delta\xi(t)$; middle, blue line, measured pressure variation from equilibrium value $\delta h(t)$; bottom, red line: flow at the valve site variation from equilibrium value $\delta Q(t)$.

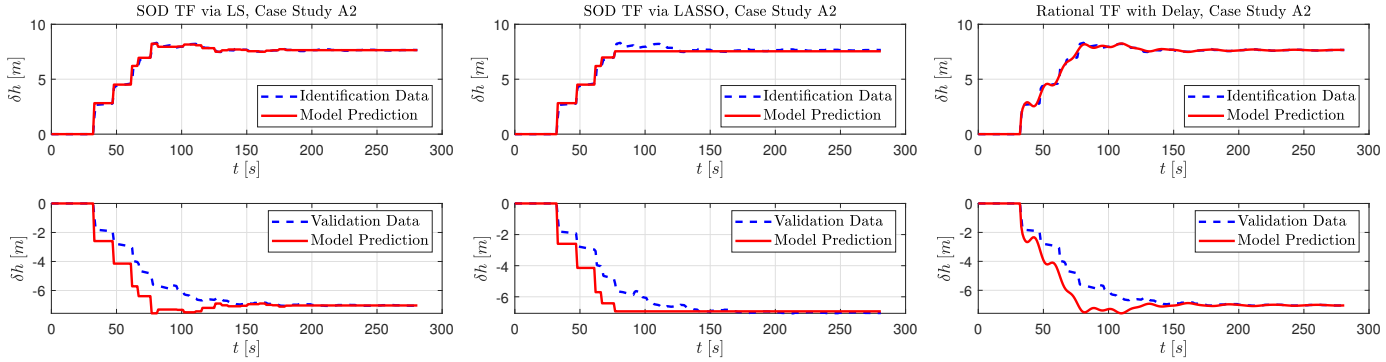

Figure 12: Case Study A2. Comparison of pressure data and model predicted pressure (Top: identification, Bottom: validation), for SOD model obtained via LS (a), SOD model obtained via LASSO (b), rational transfer function with delay (c).

Model	*RMSE*	*FIT*	*COD*
SOD via LS	2.605	0.705	0.885
SOD via LASSO	2.362	0.726	0.905
Rat. TF with Delay	2.579	0.708	0.887

Table 4: Case Study A2. Goodness of fit metrics for the Test dataset.

4.1.2. Case Study A2

The control goal for Case Study A2 is regulation of the measured pressure to a setpoint $h_{sp} = 29\ m$. The corresponding WP coincides with that of Case Study A1, i.e.: $WP_{A2} = WP_{A1}$. Step response experiments are performed around WP_{A2} to collect data and construct an identification and a validation dataset. Moreover, test data are collected by simulating a realistic valve trajectory around the working point.

The topology of Case Study A2 is described in § 2 and depicted in Figure 1. Pressure wave celerity results $c = 407.9\ m/s$. Figure 5a highlights the computed $\mathcal{T}_v^+$,$\mathcal{T}_v^-$,$\mathcal{T}_s^+$,$\mathcal{T}_s^-$ delay values over the step responses output data. As for Case Study A1, all the major pressure commutations occur very close to the expected commutation times computed from the WDN topology.

While in Case Study A1 many contributions affect the measured pressure almost simultaneously, the step response of Case Study A2 highlights the effect of the different delay classes defined in § 3.2. However, also in this case, a small set of admissible delay values could be defined by inspection of the step response pressure signal.

Once admissible values $\mathcal{T}^a$ are available, the set of discrete-time admissible delay values $\mathcal{T}^d$ can be constructed, and the associated gain identified via LS. To reduce complexity, different models are identified with the LASSO approach, with different values of the shrinkage parameter λ. The final model is then selected by inspecting the RMSE trend for both identification and validation, as function of λ. As shown by Figure 13a, both identification and validation RMSE share a similar trend, and settle to steady values for about $\lambda \leq 10$. The model associated with $\lambda = 10$ is characterised by the parameters reported in Table 3. Again, a standard rational transfer function with a single delay value is also identified: Figure 13b depicts the trend of identification and validation RMSE for different system orders. Note

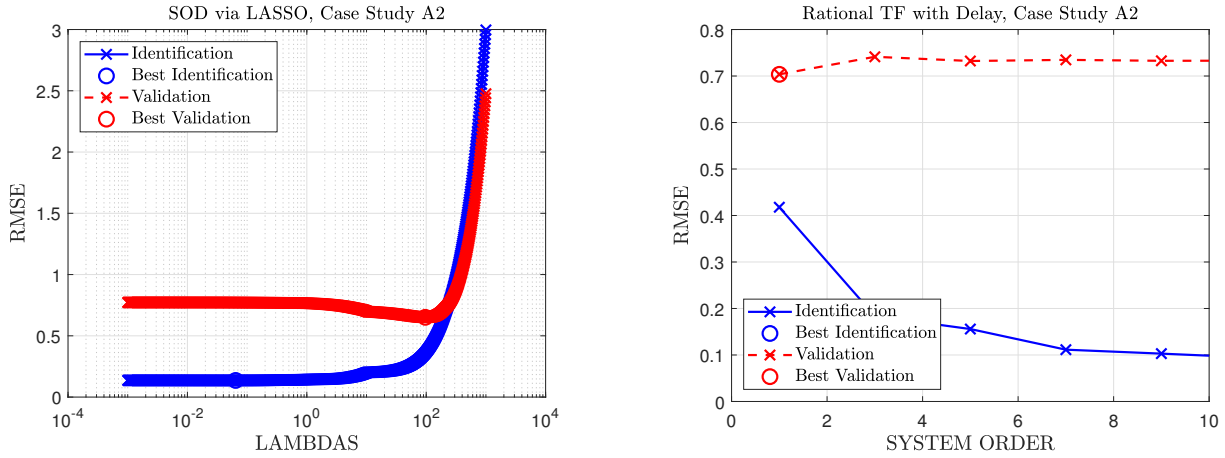

(a) (b)

Figure 13: Case Study A2. Comparison of identification (blue, solid line) and validation (red, dashed line) RMSE, for SOD models obtained via LASSO (a), and comparison of identification (blue, solid line) and validation (red, dashed line) RMSE for rational transfer functions with delay (b).

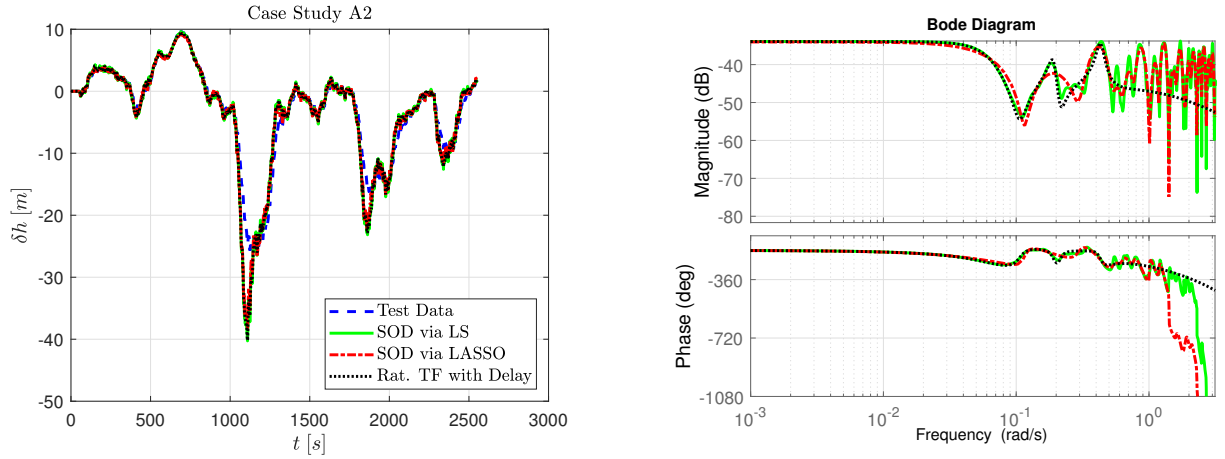

(a) (b)

Figure 14: Case Study A2. Comparison of test data (blue, dashed line), predictions for SOD model obtained via LS (green, solid line), SOD model obtained via LASSO (red, dotted-dashed line), rational transfer function model with delay (black, dotted line) (a). Comparison of Bode diagrams, depicted up to the Nyquist frequency (b).

that, while the validation RMSE trend is almost flat regardless of the system order, the identification one almost settles from order 7, which is chosen as final system order.

Figures 12a, 12b and 12c show a comparison of pressure data and model predicted pressure for both identification and validation datasets, for the three different models. As expected, the LS model prediction follows very accurately the identification data, even in its minor commutations, while LASSO model prediction only describe its main contributions. The rational transfer function with delay tries to reproduce the stair shaped signal by introducing small oscillations. As for Case Study A1, a slight mismatch exists between data and model predictions for the validation case, due to a slightly different system dynamics. The static gain is correctly estimated by all the three models, for both identification and validation data. Figure 14a shows a comparison of test data and model predictions. FIT and COD values for test data are reported in Table 4. In this case, the same considerations formulated for Case Study A1 still hold. A comparison of the Bode diagrams fo the three models is reported in Figure 14b. Note that both SOD models share a very similar diagram for both magnitude and phase, with a number of resonance peaks appearing at high frequency. In this case, the reduced number of contributions of the LASSO model with respect to the LS one result in a less accurate description of resonance peaks. The chosen rational transfer function with delay approximates the SOD Bode diagrams up to the second resonance peaks. It is important to stress the fact that a lower order transfer function may have described only the first resonance peak, while failing to reproduce the second one, which is associated with a higher magnitude and, if neglected, may cause problems in the regulator design phase [31]. Again, it must be remarked that the SOD model obtained via LASSO is the one yielding the best trade-off between model complexity and accuracy of high frequency behaviour.

p	τ_p	μ_p
1	18	-0.00797
2	21	-0.00364
3	22	-0.00041
4	23	-0.00761
5	24	-0.03583
6	25	-0.00328
7	26	-0.00045
8	27	-0.00464
9	46	-0.00158
10	55	0.00008
11	58	0.00066
12	59	0.00049
13	60	0.00093
14	61	0.00202
15	69	0.00166
16	70	0.00088
17	71	0.00006
18	85	-0.00007
19	86	-0.00137
20	87	-0.00165
21	88	-0.00091
22	89	-0.00086
23	104	0.00131
24	105	0.00020

Table 5: Case Study B. Delays and coefficients of SOD model obtained via LASSO.

Model	*RMSE*	*FIT*	*COD*
SOD via LS	0.745	0.726	0.885
SOD via LASSO	0.741	0.727	0.885
Rat. TF with Delay	0.744	0.726	0.885

Table 6: Case Study B. Goodness of fit metrics for the Test dataset.

4.1.3. Case Study B

The control goal for Case Study B is regulation of the pressure at the critical node to the setpoint $h_{sp} = 25\ m$. For Case Study B, the working point WP_B is then defined as follows:

$$WP_B = \begin{cases} \overline{\xi} = 170.45\ (i.e.\ \overline{\alpha} = 0.619) \\ \overline{H} = 39.6\ m \\ \overline{D}_1 = 0.0014\ m^3/s \\ ... \\ \overline{D}_{N_{nodes}} = 0.0007\ m^3/s \\ \overline{h} = 25\ m \\ \overline{Q} = 0.0586\ m^3/s \end{cases} \tag{46}$$

Step response experiments are performed around WP_B to collect data and construct an identification and a validation dataset. Moreover, test data are collected by simulating a realistic valve trajectory around the working point.

Case Study B topology is described in § 2 and depicted in Figure 3. Based on the above information, the methodology proposed in § 3.2.2 allows computing the sets $\mathcal{T}^{simple}$ and $\mathcal{T}^{looped}$. Figure 5c highlights the computed delay values over the step responses output data. Note that, up to $t \approx 80\ s$, it is possible to distinguish all the major pressure commutations, which occur very close to the expected commutation times computed from the WDN topology. Interestingly, such contributions belong to waves reaching the controlled node through simple paths. Also note that just few contributions are missed by the proposed procedure (e.g. $t \approx 65\ s$). These may be due to wave reflection phenomena which are not taken into account by the procedure proposed for Case Study B. At later time instants, the number of admissible delays increases noticeably, due to wave recirculation through WDN pipes, thus resulting in a much smoother signal. In this scenario, a black-box approach for the definition of admissible delay values could not be as useful as in the previous cases, where the step response shows a clear stair-shaped behaviour.

Once admissible values $\mathcal{T}^a$ are available, the set of discrete-time admissible delay values $\mathcal{T}^d$ can be constructed, and the associated gain identified via LS. In this case, the LASSO approach is fundamental to reduce the model complexity. Figure 17a depicts both identification and validation RMSE. Note that, in this case, for high values of λ, the validation RMSE is slightly lower than the identification one. This can be imputed to the static gain of the process, which appears to be different for identification and validation experiments. Models corresponding to high values of λ are in fact characterised by a low static gain, thus favouring slightly better scores in the validation metric. From a physical point of view, this is determined by the steady state value of the flow Q, which affects the steady state pressure loss through Eq. (1). The different steady state flow is in turn due to the presence of pressure dependent loss in the WDN: in the identification case, the valve is opened, resulting in a pressure increase and, eventually, an increase in Q; in the validation case, the valve is closed, causing a pressure reduction and, in turn, a flow reduction. The final model, associated with $\lambda = 0.2$, is chosen to obtain a good balance between identification and validation RMSE and is composed of 24 contributions. Model parameters are reported in Table 5, while the Bode diagram is depicted in Figure 14b. As far as the rational transfer function with a single delay value is concerned, Figure 17b depicts the trend of identification and validation RMSE for different system orders. The identification RMSE shows a standard decreasing trend, while validation RMSE reaches its minimum value from order 7, which is chosen as final system order. Figure 14a shows a comparison of test data and model predictions. FIT and COD values for test data are reported in Table 6. As already discussed in this Section, in presence of pressure dependent outflows, the valve closure affects both pressure and flow, therefore all models provide good approximations of the system dynamics, provided that the flow Q does not move too far from the WP value $\overline{Q}$. Finally, Figure 14b depicts a comparison of the Bode diagrams for the three models identified

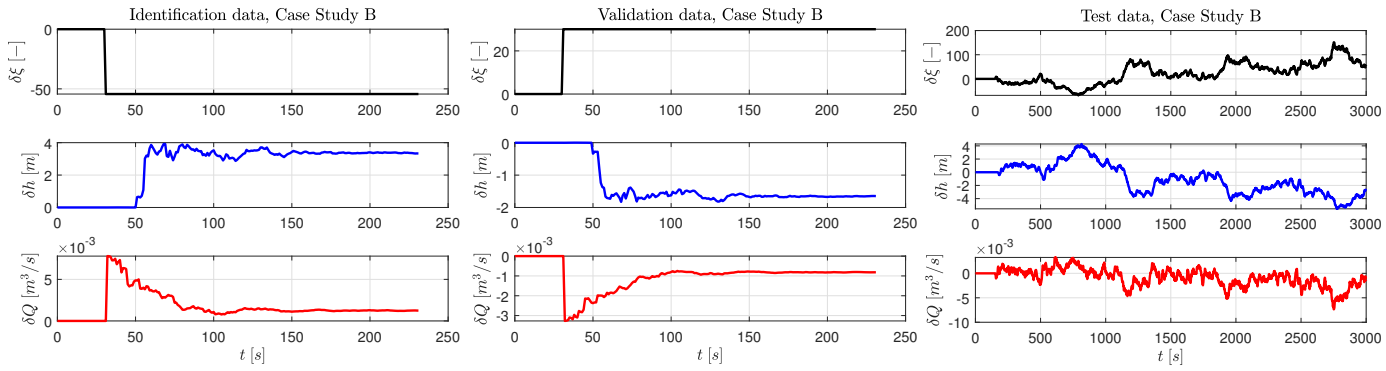

(a) (b) (c)

Figure 15: Case Study B. Model identification (a), validation (b) and test (c) data from step response experiments. Top, black line: valve head loss coefficient deviation from equilibrium value $\delta\xi(t)$; middle, blue line, measured pressure variation from equilibrium value $\delta h(t)$; bottom, red line: flow at the valve site variation from equilibrium value $\delta Q(t)$.

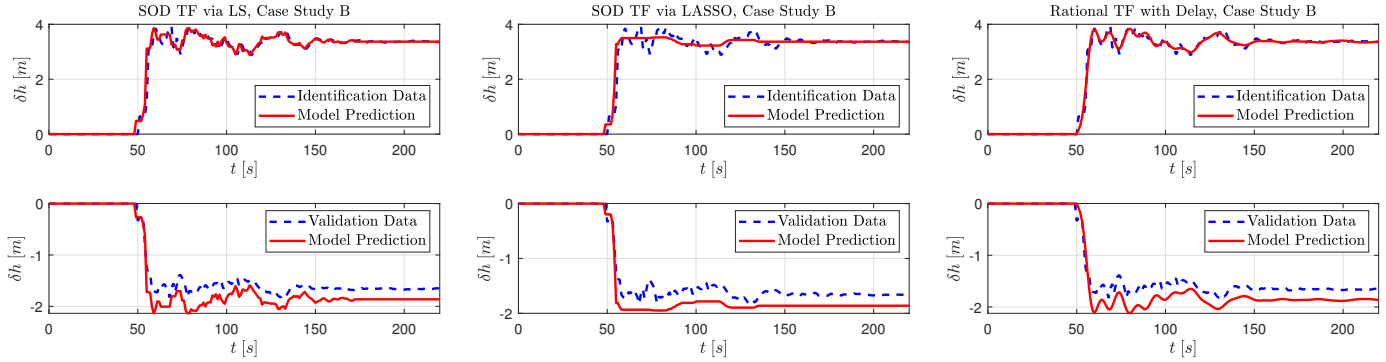

(a) (b) (c)

Figure 16: Case Study B. Comparison of pressure data and model predicted pressure (Top: identification, Bottom: validation), for SOD model obtained via LS (a), SOD model obtained via LASSO (b), rational transfer function with delay (c).

for Case Study B. In this case, the rational transfer function with delay provides a better approximation of the SOD via LS model at intermediate frequencies, well capturing the first three resonance peaks, both in terms of frequency location and peak height, while the SOD via LASSO model slightly underestimates the height of such resonance peaks. This effect results in a predicted step response which underestimates the oscillatory behaviour, which could be captured by further reducing the value of λ for the choice of the SOD model.

4.2. Regulator design and test

The model identification phase described in the previous Subsection highlighted the advantages of SOD models in case of stair-shaped system step responses. In this work, this is what happens for Case Studies A1 and A2. Moreover, SOD models can also be used in presence of complex, looped WDN topologies, as for Case Study B. This Subsection aims then at exploiting SOD models (obtained via LASSO) for the design and test of a linear regulator, by means of the bi-objective optimisation procedure introduced in § 3.3.

In all three cases cases, a LP-filtered SOD models is obtained by introducing a high frequency pole associated with a time constant $T_g = 1/\pi\ s$. Moreover, the Smith predictor for the compensation of the main delay effect is introduced, according to Eq. (44), and the regulator transfer function $R(s)$ designed based on $G'(s) = G(s)G_2(s) + P(s)$. For Case Studies A1 and A2, RT-BOOP is then setup by requiring:

$$\underline{\phi_m} = 45^\circ \quad \underline{k_m} = 15 \quad \underline{\Delta_m} = 0.5 \quad \overline{L}_{rp} = -10\ dB \tag{47}$$

and solved with a population size of 200 individuals and heuristic crossover [48], and two possible regulator structures (PI and F^1PI). For Case Studies B, RT-BOOP is instead setup by requiring:

$$\underline{\phi_m} = 60^\circ \quad \underline{k_m} = 30 \quad \underline{\Delta_m} = 0.7 \quad \overline{L}_{rp} = -10\ dB \tag{48}$$

and solved with a population size of 400 individuals and heuristic crossover [48], and two possible regulator structures (PI and F^1PI). A gain scheduling policy is then introduced for all Case Studies, with parameters values reported in § B. Finally, different simulations with the nonlinear model of the WDNs allow assessing the overall performances of the control scheme, based on the SOD models. In particular, two different metrics are adopted to quantitatively evaluate the regulation performances and the cost of control [28]. The complete definitions af the two metrics are reported in § D.

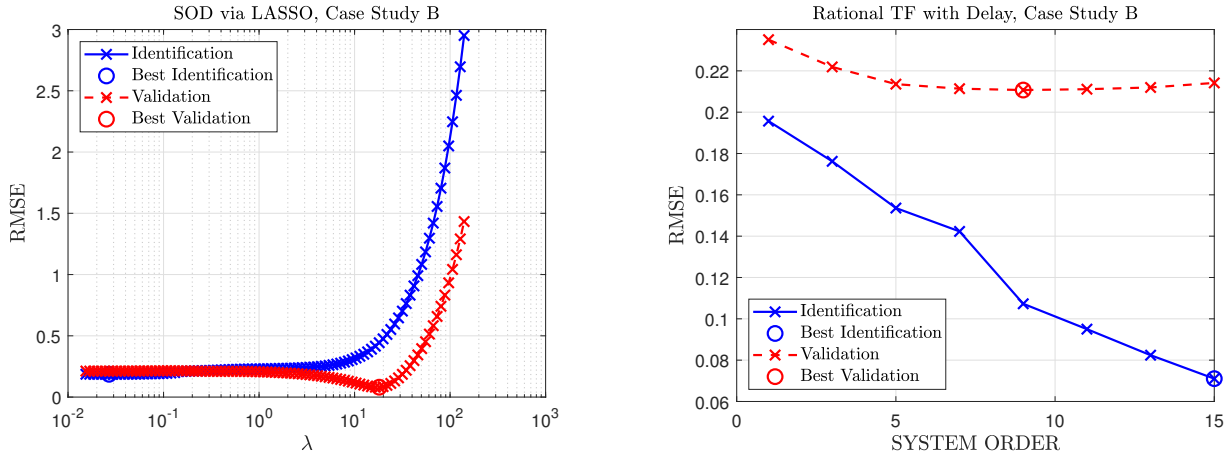

(a) (b)

Figure 17: Case Study B. Comparison of identification (blue, solid line) and validation (red, dashed line) RMSE, for SOD models obtained via LASSO (a), and comparison of identification (blue, solid line) and validation (red, dashed line) RMSE for rational transfer functions with delay (b).

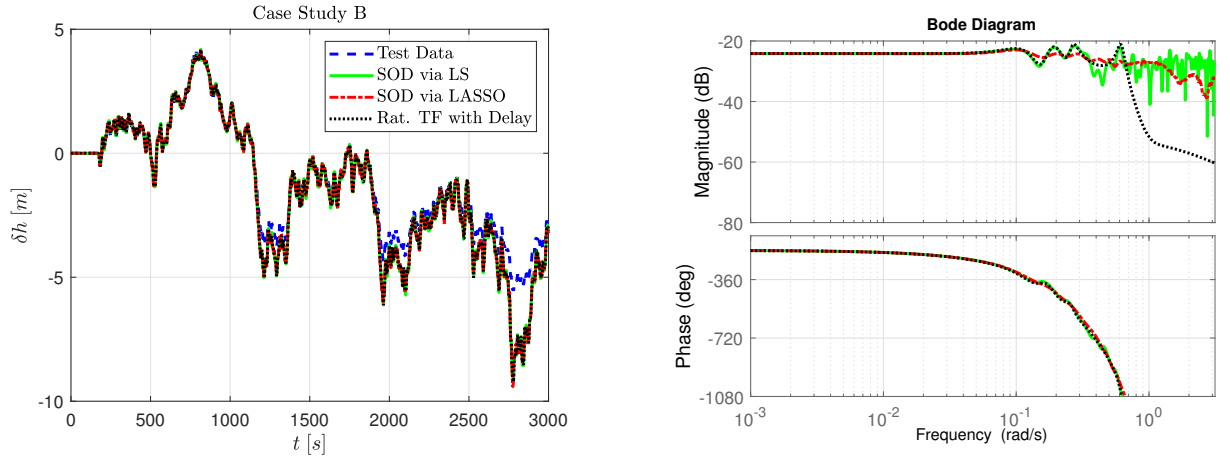

(a) (b)

Figure 18: Case Study B. Comparison of test data (blue, dashed line), predictions for SOD model obtained via LS (green, solid line), SOD model obtained via LASSO (red, dotted-dashed line), rational transfer function model with delay (black, dotted line) (a). Comparison of Bode diagrams, depicted up to the Nyquist frequency (b).

Demand Offset $[m^3/s]$	*Mean*$\lvert e(k)\rvert$ $[m]$	$\sum \lvert\Delta\alpha\rvert$ $[-]$
-0.03	1.282	14.095
0	0.836	14.628
0.05	0.636	17.729

Table 7: Case Study A1: performance of $F^1PI - SP$ algorithm for different demand offsets.

4.2.1. Case Study A1

The Bode diagram of $G'(s)$ is depicted in Figure 19a. The analysis of the phase diagram stresses how the introduction of the Smith predictor allows drastically reducing the effect of the main delay τ_1, at the price of a slight amplification of the resonance peaks located at lower frequencies, as results from the magnitude diagram. Moreover, note that the effect of the high frequency pole introduce in the SOD model only affects the transfer function characteristics for angular frequencies from about 0.5 rad/s and higher, while closed-loop bandwidths are not expected to be higher than about 0.1 rad/s, in order to obtain enough deamplification of resonance peaks. This means the the new pole should not affect too much the actual design of the loop function, while improving the solution of RT-BOOP. The resulting set of solutions, approximating the Pareto front, is depicted in Figure 20. In particular, projections in the (μ_L, ω_c) plane, (MPH, ω_c) plane and (MPH, μ_L) plane are depicted to improve readability of the plot. As expected from previous studies [28, 31], the additional filtering action introduced with F^1PI allows improving the deamplification of resonance peaks or obtaining wider closed-loop bandwidths, without exceeding the robustness margins requested for the regula-

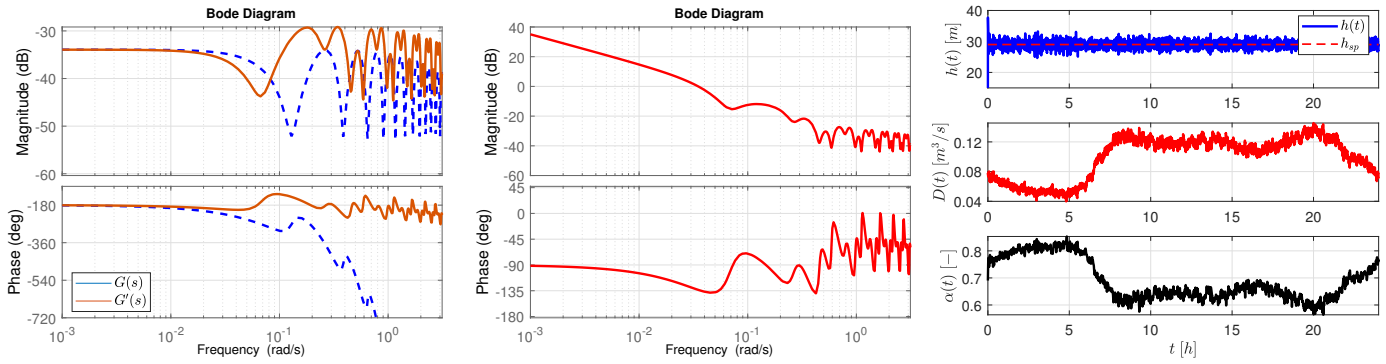

(a) (b) (c)

Figure 19: Case Study A1. Bode diagram of $G(s)$ (blue, dashed line) and $G'(s)$ (orange, solid line) (a), Bode diagram of $L(s)$ (b) and closed-loop simulation with F^1PI (c). Top: pressure $h(t)$ and pressure setpoint h_{sp}. Middle: demand $D(t)$. Bottom: valve closure $\alpha(t)$.

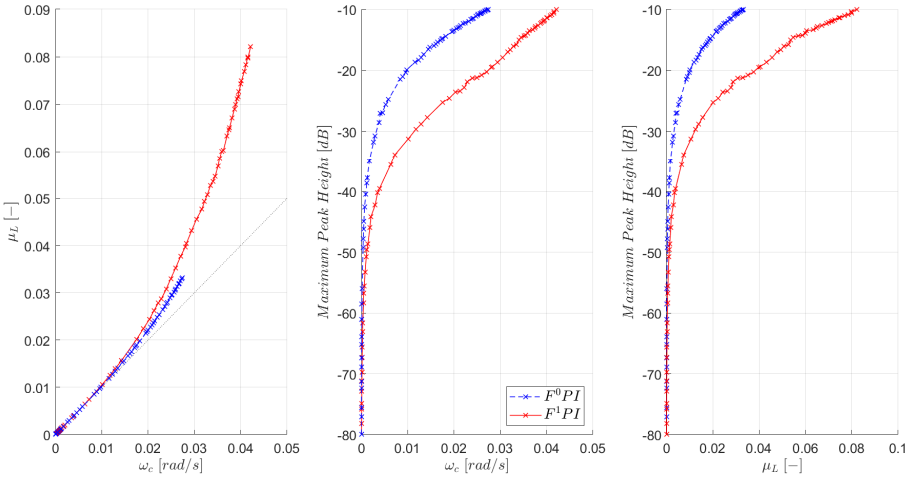

Figure 20: Case Study A1. Projections of 3D Pareto fronts resulting from the solution of the RT-BOOP in the (μ_L, ω_c) plane, (MPH, ω_c) plane and (MPH, μ_L) plane for PI (blue, dashed line) and F^1PI (red, solid line) regulator structures. The bisector line of the (μ_L, ω_c) plane is also depicted (grey, dotted line).

tor design. In particular, the F^1PI regulator tuning chosen for a whole-day simulation on the nonlinear plant corresponds to $\omega_c = 0.035\ rad/s$,$\mu_L = 0.0565$ and $MPH = -14.7\ dB$, with:

$$R(s) = \frac{-17.51s^2 - 14.06s - 2.815}{17.83s^2 + s} \tag{49}$$

This choice of a wide closed-loop bandwidth is motivated by the need to perform simulations in a demanding scenario for the control scheme. The associated robustness margins result: $\phi_m = 46.6°$,$k_m = \infty$ and $\Delta_m = 0.689$. The phase margin loss associated with discretisation with $T_s = 1\ s$ results $\phi_{ZOH} = -1°$. Figure 19b depicts the Bode diagram of the corresponding loop function $L(s)$. Note that the Bode diagram coincides with that of an integrator at low frequency, while the filtering action acts for angular frequencies close to the critical one, allowing for further resonance peak attenuation without degrading too much the disturbance rejection performances. Finally, three whole-day simulations are performed to test the regulator on the nonlinear WDN, with different demand offsets, as described in § 2. An example of simulation results is depicted in Figure 19c,

Demand Offset $[m^3/s]$	*Mean*$\lvert e(k)\rvert$ $[m]$	$\sum \lvert\Delta\alpha\rvert$ $[-]$
-0.03	1.2705	16.1829
0	0.8347	16.5569
0.05	0.6208	18.5312

Table 8: Case Study A2: performance of $F^1PI - SP$ algorithm for different demand offsets.

while a quantitative evaluation of the performances of the control scheme reported in Table 7. Results are aligned with those obtained for the same Case Study and similar regulator tunings [36].

4.2.2. *Case Study A2*

The Bode diagram of $G'(s)$ is depicted in Figure 19a. As for Case Study A1, the introduction of the Smith predictor allows

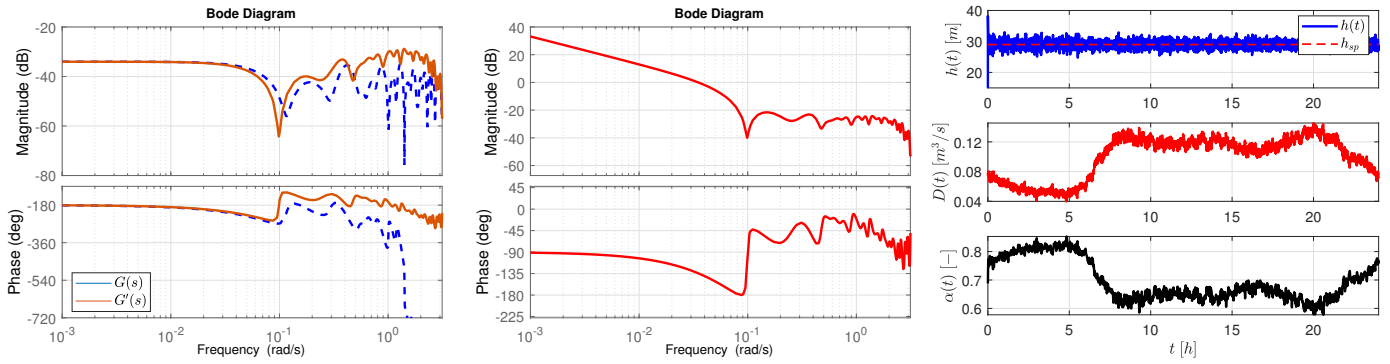

(a) (b) (c)

Figure 21: Case Study A2. Bode diagram of $G(s)$ (blue, dashed line) and $G'(s)$ (orange, solid line) (a), Bode diagram of $L(s)$ (b) and closed-loop simulation with F^1PI (c). Top: pressure $h(t)$ and pressure setpoint h_{sp}. Middle: demand $D(t)$. Bottom: valve closure $\alpha(t)$.

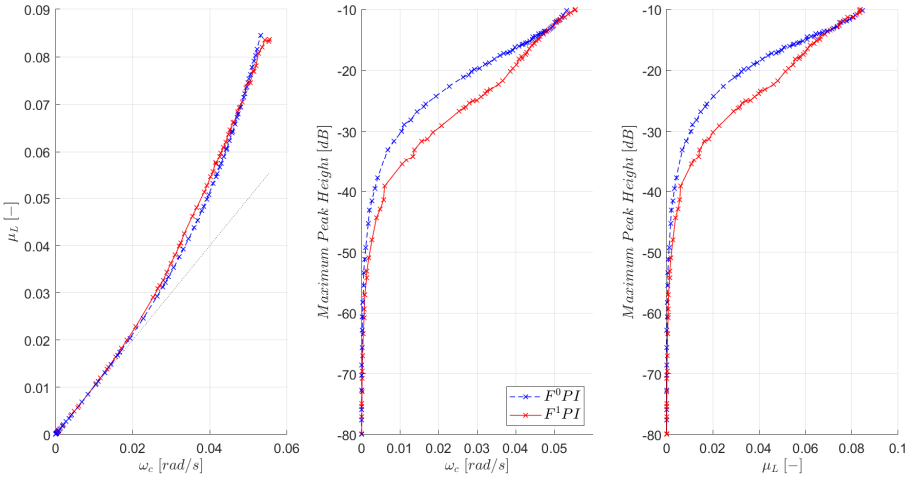

Figure 22: Case Study A2. Projections of 3D Pareto fronts resulting from the solution of the RT-BOOP in the (μ_L, ω_c) plane, (MPH, ω_c) plane and (MPH, μ_L) plane for PI (blue, dashed line) and F^1PI (red, solid line) regulator structures. The bisector line of the (μ_L, ω_c) plane is also depicted (grey, dotted line).

drastically reducing the effect of the main delay τ_1, but introduces some amplification of the resonance peaks located around $\omega \approx 1\ rad/s$. Again, the high frequency pole introduced in the SOD model pole only affects the actual design of the loop function in a minimum way. The solution of RT-BOOP is depicted in Figure 22. In particular, projections in the (μ_L, ω_c) plane, (MPH, ω_c) plane and (MPH, μ_L) plane are depicted to improve readability of the plot. In particular, the F^1PI chosen regulator tuning corresponds to $\omega_c = 0.035\ rad/s$, $\mu_L = 0.0454$ and $MPH = -22.5\ dB$, with:

$$R(s) = \frac{-19.59s^2 - 15.05s - 2.286}{12.57s^2 + s} \tag{50}$$

The associated robustness margins result: $\phi_m = 46.5°$,$k_m = 17.2$ and $\Delta_m = 0.587$. The phase margin loss associated with discretisation with $T_s = 1\ s$ results $\phi_{ZOH} = -1°$. Again, the choice of the closed-loop bandwidth allows to evaluate the performances of the control scheme in a demanding scenario.The Bode diagram of the corresponding loop function $L(s)$ is reported in Figure 21b. In addition to the considerations raised for the previous Case Study, note that the phase of $L(s)$ just reaches 180° around $\omega \approx 0.1\ rad/s$, without exceeding it. This means that, in case of phase uncertainty, the gain margin of the system may be underestimated. To conclude, the results of three whole-day simulations on the nonlinear WDN, are resumed in Table 8, and an example of simulation is depicted in Figure 21c.

4.2.3. Case Study B

The Bode diagram of $G'(s)$ is depicted in Figure 23a. In this case, as suggested by the phase diagram stresses, the introduction of the Smith predictor allows recovering part of the phase loss caused by τ_1, but introduces few dBs of amplification of the resonance peaks, as results from the magnitude diagram. This effect is slighlty more marked than in the previous Case Studies since the SOD model, derived by means of LASSO, neglects some oscillations in the step response (see Figure 16b). On the contrary, in this case, the effect on the loop function of the high frequency pole introduced in the SOD model is completely negligible. RT-BOOP solution yields the Pareto front depicted in Figure 24. In particular, projections in the (μ_L, ω_c) plane, (MPH, ω_c) plane and (MPH, μ_L) plane are

Demand Profile [−]	$Mean\|e(k)\|$ [m]	$\sum\|\Delta\alpha\|$ [−]
A	0.771	9.570
B	0.665	9.560

Table 9: Case Study B: performance of $F^1PI - SP$ algorithm for different demand profiles.

depicted. Again, the additional filtering action introduced with F^1PI allows drastically widening the closed-loop bandwidth or providing much more deamplification of resonance peaks, without exceeding the robustness margins requested for the regulator design. With the aim of obtaining loop design working close to the limit of admissible closed loop bandwidths, a F^1PI regulator tuning is chosen according to the following specifications: $\omega_c = 0.030\ rad/s$,$\mu_L = 0.038$ and $MPH = -20\ dB$,. In particular, the regulator transfer function results:

$$R(s) = \frac{-4.756s^2 - 3.438s - 0.6132}{21.47s^2 + s} \tag{51}$$

with the following associated robustness margins: $\phi_m = 60°$, $k_m = 30$ and $\Delta_m = 0.79$. The phase margin loss associated with discretisation with $T_s = 1\ s$ results $\phi_{ZOH} = -1°$. Figure 23b depicts the Bode diagram of the corresponding loop function $L(s)$. As expected from the Pareto front in Figure 24, the design correctly results in an integrator shaped function at low frequency, while the additional filtering acts aroud the critical frequency and improves the high frequency rejection abilities of the closed-lop system. Finally, in order to test the regulator on the nonlinear WDN, two whole-day simulations are performed, with two different demand profiles, as described in § 2. Simulation results are depicted in Figure 23c, while Table 9 reports a the associated values of the performance metrics. Also in this case, results can be considered satisfactory, thus stressing the effectiveness and reliability of the SOD model class also in case of complex, looped WDN topologies.

5. Discussion of results

The first goal of this paper is to provide a physically based interpretation of the complex high frequency behaviour of the plant, first highlighted in [31] by means of black-box transfer function models. As already discussed, the SOD structure allows description of the WDN dynamics based on waves travelling at finite speed, and affecting the measured pressure only at particular time intervals, which only depend on the WDN topology and on the wave speed (which in turn depends on pipe structure and fluid characteristics). The methodology proposed in this work allows computing subsets of admissible delay values, for very different WDN topologies. A comparison of the computed delay values with the actual pressure commutations instants of simulated step responses stresses the correctness of the approach. Moreover, the identification via LS estimation of the gain of each delay highlights that the interaction of multiple delayed contributions results in a high frequency behaviour characterised by a number of resonance peaks associated with low damping values, as originally obtained with black-box models. The direct comparison of the Bode diagrams of SOD and rational transfer functions with delay models suggests that both model structures can converge to a similar behaviour. However, it must be remarked that, as the degrees of freedom of the model increase, the two structures behave differently. On one hand, a rational transfer function with delay starts describing the process dynamics from low frequency and captures more and more of the high frequency one as the model order increases. This means that a low order model may not correctly capture the location and height of resonance peaks, as already discussed in [31]. On the other hand, increasing the number of SOD model contributions provides information at all frequencies, thus improving the "resolution" of the dynamic description. Hence, even a SOD model with a very low number of contributions may be extremely useful for the purpose of regulator design, since it can provide enough information about position and height of resonance peaks. As the results obtained in § 4.1 clearly highlight, this model structure is therefore particularly interesting in case of clearly stair-shaped process step responses. In this case, a variable selection approach for the model identification, such as the LASSO, results in a SOD model with very low complexity, but very rich in frequency domain information. As already introduced earlier in this work, with stair shaped step responses, it is also possible to directly obtain the values of the admissible delay from data inspection, without relying on physically based computations. On the contrary, with much smoother responses, while still being sufficiently effective and reliable, the SOD structure may not be as efficient as a rational transfer function with delay.

The second goal of this paper is to provide the control designer with an optimisation-based procedure for the design of the regulator, based on SOD transfer function models. The RT-BOOP originally formulated in [35] is then modified to remove any reference to the singularities of the loop functions, and to rely on its Bode diagram only. In particular, nominal stability is guaranteed by means of the Bode criterion [44], while minimum robustness margins are directly included in the optimisation problems as constraints. The bi-objective formulation allows to encapsulate in the optimisation problem the typical trade-off arising in the design of the loop functions. In particular, disturbance rejection and settling time properties are considered with the GBP objective function, while high frequency attenuation and control sensitivity are considered with the MPH objective function. Moreover, this approach allows explicitly considering the presence of a Smith predictor for the compensation of the main delay from the SOD model. The design procedure applied to SOD models delivered clear trends for the Pareto fronts for two different regulator structures (PI and F^1PI) from the literature [28]. Finally, the performances of the overall control scheme are evaluated with simulations on the nonlinear WDN models. The results yielded by simulations are satisfactory, and consistent with those obtained with black-box

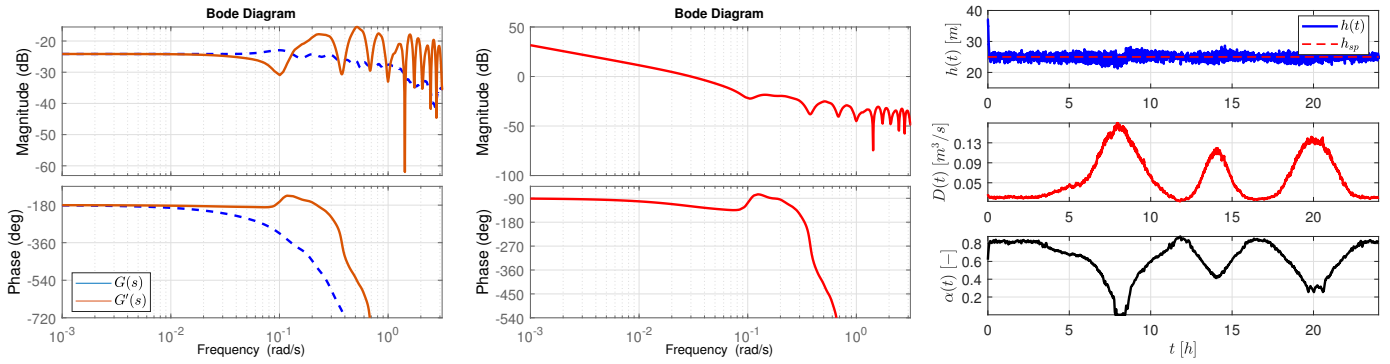

(a) (b) (c)

Figure 23: Case Study B. Bode diagram of $G(s)$ (blue, dashed line) and $G'(s)$ (orange, solid line) (a), Bode diagram of $L(s)$ (b) and closed-loop simulation with F^1PI (c). Top: pressure $h(t)$ and pressure setpoint h_{sp}. Middle: demand $D(t)$. Bottom: valve closure $\alpha(t)$.

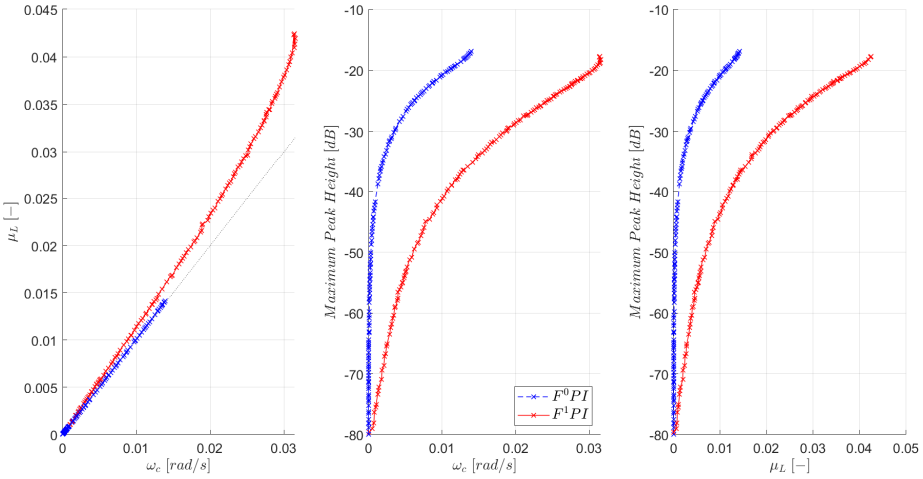

Figure 24: Case Study B. Projections of 3D Pareto fronts resulting from the solution of the RT-BOOP in the (μ_L, ω_c) plane, (MPH, ω_c) plane and (MPH, μ_L) plane for PI (blue, dashed line) and F^1PI (red, solid line) regulator structures. The bisector line of the (μ_L, ω_c) plane is also depicted (grey, dotted line).

models. Overall, the results obtained with model identification, design and test suggest that SOD models can be a useful and reliable tool for the design of regulators for pressure control in WDNs.

6. Conclusion

This paper investigates different linear, local models of WDN dynamic behaviour, in the context of service pressure regulation. Previous works highlighted that the high frequency behaviour of the plant is characterised by a number of resonance peaks: if such behaviour is not properly modelled, the stability of the closed-loop scheme may be endangered, also in view of strong process nonlineairities. In particular, this work proposes a grey-box model, based on physical considerations on WDNs unsteady flow conditions, to provide a physical justification of their complex, high frequency behaviour, and compares it to standard, black-box rational transfer functions with delay. The novel model structure consists of the sum of pure delay contributions, which mimic the effect of pressure waves travelling through the WDN pipes at finite speed. In fact, pressure waves can reach the pressure sensor after specific time intervals, which only depend on WDN structural data. A methodology for the computation of admissible time delays given WDN structural information is developed, for two very different WDN topologies, and a LASSO approach is adopted for the identification of the free parameters of the model, based on input-output step response data. The approach is validated by means of simulated step response experiments for three different Case Studies. Simulations are performed with a detailed, unsteady flow mathematical modelling of the plant. The new model structure results particularly effective and efficient in case of stair-shaped step responses of the plant. Moreover, the formulation of a bi-objective optimisation problem, based on Bode diagrams of a transfer function, allows exploiting the proposed model for the design of a linear regulator, and explicitly account for the performance vs robustness and control sensitivity trade-off. The regulators based on the new process model demonstrate to yield good performances when tested with closed-loop simulations on the nonlinear plant.

Conflict of interest

None.

References

[1] D. Sedlak, Water 4.0: the past, present, and future of the world's most vital resource, Yale University Press, 2014.

[2] D. Fiorillo, G. Galuppini, E. Creaco, F. De Paola, M. Giugni, Identification of influential user locations for smart meter installation to reconstruct the urban demand pattern, Journal of Water Resources Planning and Management 146 (8) (2020) 04020070.

[3] E. Creaco, Exploring numerically the benefits of water discharge prediction for the remote rtc of wdns, Water 9 (12) (2017) 961.

[4] E. J. M. Blokker, Stochastic water demand modelling for a better understanding of hydraulics in water distribution networks.

[5] D. Vališ, K. Hasilová, M. Forbelská, Z. Vintr, Reliability modelling and analysis of water distribution network based on backpropagation recursive processes with real field data, Measurement 149 (2020) 107026.

[6] O. Giustolisi, Water distribution network reliability assessment and isolation valve system, Journal of Water Resources Planning and Management 146 (1) (2020) 04019064.

[7] C. de Winter, V. R. Palleti, D. Worm, R. Kooij, Optimal placement of imperfect water quality sensors in water distribution networks, Computers & Chemical Engineering 121 (2019) 200–211.

[8] S. Avvedimento, S. Todeschini, C. Giudicianni, A. Di Nardo, T. Walski, E. Creaco, Modulating nodal outflows to guarantee sufficient disinfectant residuals in water distribution networks, Journal of Water Resources Planning and Management 146 (8) (2020) 04020066.

[9] E. Creaco, A. Campisano, N. Fontana, G. Marini, P. Page, T. Walski, Real time control of water distribution networks: A state-of-the-art review, Water research.

[10] A. Campisano, C. Modica, F. Musmeci, C. Bosco, A. Gullotta, Laboratory experiments and simulation analysis to evaluate the application potential of pressure remote rtc in water distributions networks, Water Research (2020) 116072.

[11] N. Fontana, M. Giugni, L. Glielmo, G. Marini, R. Zollo, Real-time control of pressure for leakage reduction in water distribution network: Field experiments, Journal of Water Resources Planning and Management 144 (3) (2017) 04017096.

[12] M. Farley, S. Trow, Losses in water distribution networks, IWA publishing, 2003.

[13] E. Creaco, T. Walski, Economic analysis of pressure control for leakage and pipe burst reduction, Journal of Water Resources Planning and Management 143 (12) (2017) 04017074.

[14] J. Thornton, A. Lambert, Managing pressures to reduce new breaks, Water 21 (December 2006) (2006) 24–26.

[15] A. Lambert, M. Fantozzi, J. Thornton, Practical approaches to modeling leakage and pressure management in distribution systems–progress since 2005, in: Proceedings of the 12th Int. Conf. on Computing and Control for the Water Industry-CCWI2013, 2013.

[16] G. Cembrano, G. Wells, J. Quevedo, R. Pérez, R. Argelaguet, Optimal control of a water distribution network in a supervisory control system, Control engineering practice 8 (10) (2000) 1177–1188.

[17] J. M. Grosso, J. M. Maestre, C. Ocampo-Martinez, V. Puig, On the assessment of tree-based and chance-constrained predictive control approaches applied to drinking water networks, IFAC Proceedings Volumes 47 (3) (2014) 6240 – 6245, 19th IFAC World Congress.

[18] J. Grosso, C. Ocampo-Martínez, V. Puig, B. Joseph, Chance-constrained model predictive control for drinking water networks, Journal of process control 24 (5) (2014) 504–516.

[19] J. M. Grosso, P. Velarde, C. Ocampo-Martinez, J. M. Maestre, V. Puig, Stochastic model predictive control approaches applied to drinking water networks, Optimal Control Applications and Methods 38 (4) (2017) 541–558.

[20] C. Ocampo-Martinez, D. Barcelli, V. Puig, A. Bemporad, Hierarchical and decentralised model predictive control of drinking water networks: Application to barcelona case study, IET control theory & applications 6 (1) (2012) 62–71.

[21] C. Ocampo-Martinez, V. Puig, G. Cembrano, J. Quevedo, Application of predictive control strategies to the management of complex networks in the urban water cycle [applications of control], IEEE Control Systems 33 (1) (2013) 15–41.

[22] R. Toro, C. Ocampo-Martínez, F. Logist, J. V. Impe, V. Puig, Tuning of predictive controllers for drinking water networked systems, IFAC Proceedings Volumes 44 (1) (2011) 14507 – 14512, 18th IFAC World Congress.

[23] E. Salomons, M. Housh, A practical optimization scheme for real-time operation of water distribution systems, Journal of Water Resources Planning and Management 146 (4) (2020) 04020016.

[24] F. Pugliese, F. De Paola, N. Fontana, M. Giugni, G. Marini, Experimental characterization of two pumps as turbines for hydropower generation, Renewable energy 99 (2016) 180–187.

[25] N. Fontana, M. Giugni, L. Glielmo, G. Marini, Real time control of a prototype for pressure regulation and energy production in water distribution networks, Journal of Water Resources Planning and Management 142 (7) (2016) 04016015.

[26] N. Fontana, M. Giugni, L. Glielmo, G. Marini, R. Zollo, Use of hydraulically operated prvs for pressure regulation and power generation in water distribution networks, Journal of Water Resources Planning and Management 146 (7) (2020) 04020047.

[27] E. Creaco, G. Galuppini, A. Campisano, C. Ciaponi, G. Pezzinga, A bi-objective approach for optimizing the installation of pats in systems of transmission mains, Water 12 (2) (2020) 330.

[28] G. Galuppini, E. Creaco, C. Toffanin, L. Magni, Service pressure regulation in water distribution networks, Control Engineering Practice 86 (2019) 70–84.

[29] N. Fontana, M. Giugni, L. Glielmo, G. Marini, F. Verrilli, Real-time control of a prv in water distribution networks for pressure regulation: Theoretical framework and laboratory experiments, Journal of Water Resources Planning and Management 144 (1) (2017) 04017075.

[30] A. Campisano, C. Modica, L. Vetrano, Calibration of proportional controllers for the rtc of pressures to reduce leakage in water distribution networks, Journal of Water Resources Planning and Management 138 (4) (2011) 377–384.

[31] G. Galuppini, L. Magni, E. Creaco, Stability and robustness of real-time pressure control in water distribution systems, Journal of Hydraulic Engineering 146 (4) (2020) 04020023.

[32] B. Ulanicki, P. Skworcow, Why prvs tends to oscillate at low flows, Procedia Engineering 89 (2014) 378–385.

[33] T. Janus, B. Ulanicki, Effects of sampling on stability and performance of electronically controlled pressure-reducing valves, Journal of Water Resources Planning and Management 147 (3) (2021) 04021003.

[34] T. Hastie, R. Tibshirani, J. Friedman, The elements of statistical learning: data mining, inference, and prediction, Springer Science & Business Media, 2009.

[35] G. Galuppini, E. Creaco, L. Magni, Bi-objective optimisation based tuning of pressure control algorithms for water distribution networks, Control Engineering Practice 104 (2020) 104632.

[36] G. Galuppini, E. Creaco, L. Magni, A gain scheduling approach to improve pressure control in water distribution networks, Control Engineering Practice 103 (2020) 104612.

[37] T. Janus, B. Ulanicki, Hydraulic modelling for pressure reducing valve controller design addressing disturbance rejection and stability properties, Elsevier, 2017.

[38] E. Creaco, A. Campisano, M. Franchini, C. Modica, Unsteady flow modeling of pressure real-time control in water distribution networks, Journal of Water Resources Planning and Management 143 (9) (2017) 04017056.

[39] V. L. Streeter, E. B. Wylie, K. W. Bedford, Fluid mechanics, wcb (1998).

[40] C. Ciaponi, L. Franchioli, E. Murari, S. Papiri, Procedure for defining a pressure-outflow relationship regarding indoor demands in pressure-driven analysis of water distribution networks, Water resources management 29 (3) (2015) 817–832.

[41] G. Pezzinga, Evaluation of unsteady flow resistances by quasi-2d or 1d models, Journal of Hydraulic Engineering 126 (10) (2000) 778–785.

[42] E. Creaco, F. De Paola, D. Fiorillo, M. Giugni, Bottom-up generation of water demands to preserve basic statistics and rank cross-correlations of measured time series, Journal of Water Resources Planning and Management 146 (1) (2020) 06019011.

[43] E. Creaco, G. Galuppini, A. Campisano, M. Franchini, Bottom-up gener-

ation of peak demand scenarios in water distribution networks, Sustainability 13 (1) (2021) 31.
[44] D. E. Seborg, D. A. Mellichamp, T. F. Edgar, F. J. Doyle III, Process dynamics and control, John Wiley & Sons, 2010.
[45] J. Y. Yen, Finding the k shortest loopless paths in a network, management Science 17 (11) (1971) 712–716.
[46] L. Magni, R. Scattolini, Advanced and multivariable control, Pitagora, 2014.
[47] K. Deb, A. Pratap, S. Agarwal, T. Meyarivan, A fast and elitist multiobjective genetic algorithm: Nsga-ii, IEEE transactions on evolutionary computation 6 (2) (2002) 182–197.
[48] K. Deb, Multi-objective optimization using evolutionary algorithms, Vol. 16, John Wiley & Sons, 2001.
[49] L. Ljung, System identification toolbox: for use with MATLAB: user's guide, Math Works, 1991.

Appendices

A. Wave celerity

The wave celerity c can be related to known or measurable physical quantities of water and of the pipe as follows:

$$c = \left(\frac{\frac{\epsilon}{\zeta}}{1 + \frac{\epsilon d}{E s}} \right)^{\frac{1}{2}} \tag{52}$$

where ϵ $[Pa]$ and ζ $[kg/m^3]$ are water bulk modulus and density; E $[Pa]$, d $[m]$ and s $[m]$ are pipe modulus of elasticity, diameter and thickness.

B. Gain Scheduling

For Case Studies A1 and A2, the following parameters are adopted for the gain scheduling policy:

$$\alpha^* = 0.55 \tag{53}$$
$$\mu^*_{ratio} = 0.1 \tag{54}$$
$$p = 4 \tag{55}$$

For Case Studies B, the gain scheduling policy is instead based on the following parameter values:

$$\alpha^* = 0.5 \tag{56}$$
$$\mu^*_{ratio} = 0.1 \tag{57}$$
$$p = 6 \tag{58}$$

For further details about gain scheduling policy, refer to [36]. It must be remarked that, for sake of comparison, the gain scheduling parameter values adopted in this work are consistent with those of [36, 35].

C. Bode criterion

Consider a generic loop gain function $L(s)$. Let $L(s)$ have poles with non-positive real part only, and let the Bode diagram of $|L(j\omega)|$ cross the 0 dB axis only once, from above. Then, by defining as μ_L the gain of $L(s)$ and as ϕ_m the phase margin, the negative feedback system $F(s) = L(s)/(1 + L(s))$ is asymptotically stable iif $\mu_L > 0$ and $\phi_m > 0$.

D. Performance metrics

The results of simulations are evaluated according to the following metrics:

- $Mean|e(k)|$ $[m]$. The *regulation error*, which evaluates the proximity of the pressure to the desired setpoint.
- $\sum |\Delta\alpha(k)|$ $[-]$. The *cost of control*, which impacts on the energy required to perform regulation and on wear of actuators.

where $h(k)$ is the measured pressure, h_{sp} is the pressure setpoint, $\alpha(k)$ is the valve closure and $\Delta\alpha(k) = \alpha(k) - \alpha(k-1)$ is the variation of the valve closure over a single sampling time. Let $e(k) = h(k) - h_{sp}$ be the error of the controlled pressure head at time instant k. All signals are sampled with sampling time of 1 s.